

# Journal of Materials Chemistry A

Materials for energy and sustainability

Accepted Manuscript

This article can be cited before page numbers have been issued, to do this please use: D. Bekele Tekliye and G. Sai Gautam, *J. Mater. Chem. A*, 2024, DOI: 10.1039/D4TA02426E.



This is an Accepted Manuscript, which has been through the Royal Society of Chemistry peer review process and has been accepted for publication.

Accepted Manuscripts are published online shortly after acceptance, before technical editing, formatting and proof reading. Using this free service, authors can make their results available to the community, in citable form, before we publish the edited article. We will replace this Accepted Manuscript with the edited and formatted Advance Article as soon as it is available.

You can find more information about Accepted Manuscripts in the [Information for Authors](#).

Please note that technical editing may introduce minor changes to the text and/or graphics, which may alter content. The journal's standard [Terms & Conditions](#) and the [Ethical guidelines](#) still apply. In no event shall the Royal Society of Chemistry be held responsible for any errors or omissions in this Accepted Manuscript or any consequences arising from the use of any information it contains.

# Journal Name

## ARTICLE TYPE

Cite this: DOI: 00.0000/xxxxxxxxxx

# Fluoride Frameworks as Potential Calcium Battery Cathodes<sup>†</sup>

Dereje Bekele Tekliye<sup>a</sup> and Gopalakrishnan Sai Gautam<sup>\*a</sup>

Received Date

Accepted Date

DOI: 00.0000/xxxxxxxxxx

Calcium batteries (CBs) are potential next-generation energy storage devices, offering a promising alternative to lithium-ion batteries due to their theoretically high energy density, better safety, and lower costs associated with the natural abundance of calcium. However, the limited availability of positive electrode (cathode) materials has constrained the development of CBs so far. Given the similar ionic radii of  $\text{Na}^+$  and  $\text{Ca}^{2+}$ , structures that are effective at reversibly intercalating  $\text{Na}^+$  may be able to reversibly intercalate  $\text{Ca}^{2+}$  as well. In this context, transition metal fluorides (TMFs) exhibiting weberite and perovskite structures that are known for intercalating  $\text{Na}^+$  form an interesting set of possible CB cathode frameworks. Thus, we use first principles calculations to explore weberite and perovskite TMFs as CB cathodes, of compositions  $\text{Ca}_x\text{M}_2\text{F}_7$  and  $\text{Ca}_x\text{MF}_3$ , respectively, where  $\text{M} = \text{Ti}, \text{V}, \text{Cr}, \text{Mn}, \text{Fe}, \text{Co}, \text{or Ni}$ . We systematically evaluate key cathode properties, including ground state structure, average Ca-intercalation voltage, thermodynamic stability (at 0 K), theoretical capacity, and  $\text{Ca}^{2+}$  migration barriers. Importantly, we identify  $\text{Ca}_x\text{Cr}_2\text{F}_7$  and  $\text{Ca}_x\text{Mn}_2\text{F}_7$  weberite frameworks as promising Ca-cathodes. Our study not only unveils potential CB cathodes but also paves the way for further advancement in TMF-based intercalation cathodes, diversifying the chemical space for next-generation energy storage systems.

## 1 Introduction

The ubiquity of rechargeable Li-ion batteries (LIBs), with their high energy and power density, has emerged as the predominant energy source for numerous applications ranging from portable electronics, electric vehicles, and stationary energy storage.<sup>1–6</sup> However, the growing demand for LIBs across a wide variety of applications raises concern about Li (also Co and Ni) resource availability and associated supply-chain constraints<sup>7</sup>, necessitating an exploration of alternate solutions to the LIB technology. Off-late, there is growing interest in Calcium batteries (CBs) as a potential next-generation battery technology due to: (i) the low standard reduction potential of Ca (-2.87 V versus standard hydrogen electrode, SHE) approaching that of Li (-3.04 V versus SHE), (ii) the multivalent nature of  $\text{Ca}^{2+}$ , which shuttles two valence electrons at a time, combined with the use of Ca-metal as anode, which can result in an increased volumetric energy density<sup>8–13</sup>, (iii) CBs utilize Ca, which is more abundant than Li (Ca: 4.2% versus Li: 0.002% of earth's crust<sup>14</sup>), potentially making

CBs less expensive and more sustainable than LIBs.

Despite the inherent advantages, the development of CBs is constrained by the need for suitable electrolytes and positive electrodes (cathodes). While stripping and plating Ca-metal at the negative electrode (anode) has encountered challenges due to electrolyte decomposition<sup>11,15</sup>, recent advances in the electrolyte design have enabled efficient Ca plating/stripping with the formation of a protective layer enhancing electrochemical performance.<sup>16–19</sup> However, the lack of suitable cathode candidates, namely lack of thermodynamic and/or cyclic stability,<sup>13</sup> and poor  $\text{Ca}^{2+}$  diffusion,<sup>20</sup> continues to hinder the development of practical CBs.

Previous studies have employed both experimental and computational techniques to explore select chemistries as possible CB cathodes. The set of inorganic cathodes that have been reported with Ca so far include  $\text{CaMo}_6\text{X}_8$  ( $\text{X} = \text{S}, \text{Se}, \text{or Te}$ ),<sup>21</sup>  $\text{VOPO}_4 \cdot 2\text{H}_2\text{O}$ ,<sup>22</sup>  $\text{Ca}_x\text{V}_2\text{O}_5$ ,<sup>23–27</sup>  $\text{CaV}_2\text{O}_4$ ,<sup>28,29</sup>  $\text{CaMn}_2\text{O}_4$ ,<sup>30</sup>  $\text{MoO}_3$ ,<sup>31–33</sup>  $\text{NH}_4\text{V}_4\text{O}_{10}$ ,<sup>34</sup>  $\text{CaCo}_2\text{O}_4$ ,<sup>35,36</sup>  $\text{NaFePO}_4\text{F}$ ,<sup>37</sup>  $\text{TiS}_2$ ,<sup>38</sup>  $\text{CaV}_6\text{O}_{16} \cdot 2.8\text{H}_2\text{O}$ ,<sup>39</sup> Prussian-blue analogues (PBA)<sup>40–44</sup>, and other polyanionic frameworks.<sup>45–48</sup> However, only a select few of these compounds show reasonable electrochemical performance, with most suffering from inadequate cyclic stability, poor Ca-ion diffusion, and large volume changes during charge/discharge. For instance,  $\text{VOPO}_4 \cdot 2\text{H}_2\text{O}$  demonstrates reasonable electrochemical performance against Ca-containing electrolytes,<sup>22</sup> yet its susceptibility to proton intercalation and the undesirable

<sup>a</sup> Department of Materials Engineering, Indian Institute of Science, Bengaluru, 560012, Karnataka, India; E-mail: saigautamg@iisc.ac.in

<sup>†</sup> Electronic Supplementary Information (ESI) available: Projector augmented wave potentials used, structural features of orthorhombic and trigonal weberites, ground state Ca-vacancy configurations in both weberites and perovskites, 0 K phase diagrams, and minimum energy pathways of  $\text{Ca}^{2+}$  migration in select structures. See DOI: 00.0000/00000000.

effects of water in organic electrolytes pose challenges for practical cell applications.<sup>49</sup>

Recently, Chando et al.<sup>30</sup> explored the post-spinel phase of CaMn<sub>2</sub>O<sub>4</sub> as CB-cathode candidate using both experiments and density functional theory (DFT)<sup>50,51</sup> calculations, and reported a low cycling capacity of 52 mAh/g at a rate of C/33. Prabakar et al.<sup>26</sup> used a water-free  $\beta$ -phase Ca<sub>0.14</sub>V<sub>2</sub>O<sub>5</sub> as a Ca-cathode and reported a reversible capacity of  $\sim$ 247 mAh/g. The authors stated that unlike conventional layered  $\beta$ -V<sub>2</sub>O<sub>5</sub> and  $\delta$ -Ca<sub>x</sub>V<sub>2</sub>O<sub>5</sub> $\cdot$ nH<sub>2</sub>O cathodes, the  $\beta$ -phase facilitates efficient insertion/extraction of Ca ions, contributing to improved cyclic stability and minimal dimensional changes during charge/discharge cycles.<sup>26</sup>

In terms of polyanionic materials, Vaughney and co-workers<sup>45</sup> reported two phosphates, namely sodium superionic conductor (NaSICON) (NaV<sub>2</sub>(PO<sub>4</sub>)<sub>3</sub>) and olivine (FePO<sub>4</sub>), as high-voltage cathodes for room-temperature CBs. NaV<sub>2</sub>(PO<sub>4</sub>)<sub>3</sub> demonstrates stable cycling with reversible intercalation of  $\sim$ 0.6 mol of Ca<sup>2+</sup> at 3.2 V vs. Ca, while FePO<sub>4</sub> exhibits reversible intercalation of  $\sim$ 0.2 mol of Ca<sup>2+</sup> at 2.9 V. Subsequently, Kang and co-workers<sup>47</sup> reported a successful extraction/insertion of Ca from/into Na<sub>0.5</sub>VPO<sub>4.8</sub>F<sub>0.7</sub>, exhibiting exceptional cycling stability with 90% capacity retention over 500 cycles and 87 mAh/g capacity. Additionally, Nazar and coworkers<sup>52</sup> investigated the Ca–Na dual cation system, using experimental and computational methods to understand the phase evolution and kinetics of Ca<sub>x</sub>NaV<sub>2</sub>(PO<sub>4</sub>)<sub>3</sub> that takes place during Ca<sup>2+</sup> cycling. The authors reported a reversible Ca<sup>2+</sup> cycling capacity being limited to be  $x \approx 0.65$  in Ca<sub>x</sub>NaV<sub>2</sub>(PO<sub>4</sub>)<sub>3</sub>, attributing the limit due to phase separation into Na-rich and Ca-rich phases. Also, the authors demonstrated that Na<sup>+</sup> migration within the host framework facilitates neighboring Ca<sup>2+</sup> migration, enabling reversible electrochemical activity.

With respect to recent computational identification of promising Ca-cathodes, Lu et al.<sup>28</sup> identified two promising Ca-cathode compositions through a DFT-based high-throughput screening considering average voltages, thermodynamic stability, and migration barriers, namely, post-spinel-CaV<sub>2</sub>O<sub>4</sub> and layered-CaNb<sub>2</sub>O<sub>4</sub>. While a subsequent experimental investigation by Palacín, Arroyo-de Dompablo and co-workers<sup>29</sup> showed promise for reversible Ca intercalation in CaV<sub>2</sub>O<sub>4</sub>, further optimization of the electrode framework is imperative. Additionally, we performed an extensive screening study of NaSICON frameworks as potential Ca-cathodes.<sup>48</sup> Specifically, we used first principles calculations to determine the ground state structure, average intercalation voltage, 0 K thermodynamic stability, and migration barrier, using which we identified three promising candidate Ca-cathodes, namely, Ca<sub>x</sub>V<sub>2</sub>(PO<sub>4</sub>)<sub>3</sub>, Ca<sub>x</sub>Mn<sub>2</sub>(SO<sub>4</sub>)<sub>3</sub>, and Ca<sub>x</sub>Fe<sub>2</sub>(SO<sub>4</sub>)<sub>3</sub>. Experimental realization of these predicted Na-SICONs, except for Ca<sub>x</sub>V<sub>2</sub>(PO<sub>4</sub>)<sub>3</sub>, is pending.

In the context of using anion chemistry to boost energy density of cathodes, Fluorine's high electronegativity triggers a strong inductive effect on transition-metal (TM) ions within the cathode.<sup>53</sup> As a result of this inductive effect, the electron density on the TM redox center reduces, resulting in a better response to addition or removal of electrons, or a higher voltage with the (de)intercalation of an electroactive ion.<sup>54</sup> In addition, the lower

molar mass of F compared to polyanionic groups (e.g., phosphates) can enhance the gravimetric capacity of a given cathode. Thus, fluorine-based frameworks can exhibit higher voltages, on average, compared to oxide or other halide frameworks. As a result, researchers typically utilize F<sup>-</sup> to substitute anionic sites or polyanionic groups, completely/partially, yielding better cathode materials with enhanced properties.<sup>47,55-58</sup>

Fluorides as a chemical space are a promising, yet overlooked class of host materials as cathodes in intercalation-based electrochemical energy storage systems, especially in CBs. A few fluoride compounds, such as perovskite-type NaMF<sub>3</sub> (M = Fe, Mn, Ni, and Co), have been investigated as cathodes for sodium-ion batteries (NIBs).<sup>59,60</sup> NaFeF<sub>3</sub> showed an initial capacity of 130 mAh<sup>-1</sup>, yet suffered from high polarization and capacity fading, while the initial charge capacity of NaMnF<sub>3</sub>, NaNiF<sub>3</sub> and NaCoF<sub>3</sub> was limited to 40 mAh<sup>-1</sup>, largely attributable to side reaction as later demonstrated by Dimov et al.<sup>61</sup> While Ca is known to occupy the perovskite framework among oxides,<sup>62,63</sup> fluorine-based perovskites have not been rigorously explored for CBs.

Weberite-type fluorides (typically Fe-containing), known for their robust three-dimensional open framework interconnected by FeF<sub>6</sub> octahedra, have been explored computationally as NIB cathodes by Euchner et al.<sup>64</sup> Moreover, weberites can be synthesized from fluoride precursors using topochemical wet chemistry routes, which employ lower temperatures compared to solid-state synthesis routes.<sup>65,66</sup> Recently, Park et al.<sup>67</sup> investigated trigonal-type fluoride weberite (Na<sub>2</sub>Fe<sub>2</sub>F<sub>7</sub>), using experimental and computational methods. The authors demonstrated a high capacity of 184 mAh/g at C/20 (1C = 184 mA g<sup>-1</sup>), which approaches the theoretical capacity of the weberite and reported a capacity retention over 88% of the initial capacity at 2C after 1000 cycles along with an average operating voltage of  $\sim$ 3.1 V. Park et al. attributed this exceptional electrochemical performance to preventing structural changes during Na (de)intercalation and facile Na<sup>+</sup> diffusion. Note that the similarity in size between Na<sup>+</sup> and Ca<sup>2+</sup> (116 and 114 pm in an octahedral coordination environment surrounded by O<sup>2-</sup>, respectively<sup>68,69</sup>) indicates that cathodes with reversible Na-intercalation may hold promise as CB cathodes as well. Thus, fluoride frameworks, specifically with the weberite and perovskite structures, could be potential Ca-cathodes.

In this work, we use DFT-based calculations to systematically explore the chemical space of weberite- and perovskite-type fluorides, with chemical formula of Ca<sub>x</sub>M<sub>2</sub>F<sub>7</sub> and Ca<sub>x</sub>MF<sub>3</sub>, respectively, as potential CB cathodes. Here, M represents a redox active 3d transition metal, including Ti, V, Cr, Mn, Fe, Co, or Ni, while x represents the Ca composition within a range of 0  $\leq$  x  $\leq$  1.5 for weberites and 0  $\leq$  x  $\leq$  0.5 for perovskites. We calculate the ground state structure (including the stable Ca-vacancy arrangement), 0 K thermodynamic stability, average Ca intercalation voltage and Ca<sup>2+</sup> migration barriers upon Ca (de)insertion in the weberite and perovskite fluorides. Importantly, our systematic screening identifies Ca<sub>x</sub>Cr<sub>2</sub>F<sub>7</sub> and Ca<sub>x</sub>Mn<sub>2</sub>F<sub>7</sub> weberites as promising cathode candidates for CBs. Our study marks the first extensive exploration of fluoride frameworks as potential intercalation-type Ca-cathode materials, which can hopefully aid in the practical development of energy dense CBs.

## 2 Results

### 2.1 Structural Features

#### 2.1.1 Weberites

The weberite structure derives its name from the parent compound, namely the mineral  $\text{Na}_2\text{MgAlF}_7$ , and typically crystallizes in an orthorhombic structure<sup>70</sup> with a space group of *Imma* (panels a and b of Figure 1). The weberite framework is considered as a type of anion-deficient fluorite superstructure with a general stoichiometry of  $\text{A}^{(4a)}\text{A}'^{(4d)}\text{M}^{(4b)}\text{M}'^{(4c)}\text{F}_7^{(4e,8h,16j)}$ . A and A' usually represent Na occupying two different crystallographic sites, represented by orange (Na1 or 4a sites) and blue (Na2 or 4d) spheres in Figure 1a and b. M and M' represent TM cation with a +2 and a +3 oxidation state, respectively, and are represented by green and purple octahedra in Figure 1. Note that the A and A' represent possible sites for Ca occupation in Ca-containing weberites. The conventional cell of the orthorhombic weberite (Figure 1a) consists of four  $\text{A}_2\text{M}_2\text{F}_7$  ( $\text{A} = \text{Na/Ca}$ ) formula units, with the  $\text{MF}_6$  and  $\text{M}'\text{F}_6$  octahedra sharing corners to form a three-dimensional framework. The primitive cell of the orthorhombic weberite (Figure 1b) has two  $\text{A}_2\text{M}_2\text{F}_7$  formula units. The fluorine atoms, which are represented by grey spheres, occupy three different Wyckoff positions, namely F1 (4e), F2 (8h) and F3 (16j).

Both Na1 and Na2 sites coordinate with 6+2 with neighboring fluorine atoms, with Na1 exhibiting a hexagonal bipyramidal coordination and Na2 displaying a distorted cubic (or square prism) coordination. While Na1 coordinates with all three types of F sites, Na2 coordinates with only F1 and F2. The Na2 polyhedra are interconnected via edge-sharing, resulting in a series of chains along [100], as shown in Figure S1a of the supporting information (SI). On the other hand, the Na1 polyhedra share corners among each other along [010] (Figure S1b), with the Na1 polyhedra also sharing some of their edges with Na2 polyhedra (Figure S1a). Note that there exists another orthorhombic weberite structure, with space group *Pmn*<sub>b</sub>, which is considered to be a modification of the *Imma* weberite via tilting of the Na1 polyhedra resulting in a set of non-corner-sharing pentagonal bipyramidal polyhedra (Figure S1c). We will not be considering the distorted *Pmn*<sub>b</sub> version of the weberite structure further in our work.

Interestingly, the *Imma* weberite framework can be considered as a repeated stacking of slabs made of (011) planes. Each slab consists of two distinct layers, namely  $\text{A}_3\text{M}$  (A-rich layer) and  $\text{AM}_3$  (TM-rich layer), forming an 'AA' stacking sequence, as depicted in Figure S2a. In turn, each layer exhibits a Kagome-like network where majority cations (A in  $\text{A}_3\text{M}$  and M in  $\text{AM}_3$ ) form a continuous network, while minority cations occupy the Kagome ring centers as illustrated in Figure S2b,c.

In addition to the orthorhombic crystal structure, weberite can exist as a trigonal and a monoclinic polymorph, which differ in their stacking sequence of the Kagome-type layers.<sup>71,72</sup> Figure 1c depicts the conventional cell of trigonal weberite of space group *P3<sub>1</sub>21* and consisting of six formula units of  $\text{A}_2\text{M}_2\text{F}_7$ , depicted including the Wyckoff notation as  $\text{A}_2^{(6c)}\text{M}^{(3a)}\text{M}'^{(3b)}\text{M}''^{(6c)}\text{F}_7^{(6c)}$ . In trigonal weberites, there are two distinct sites for trivalent cations

M/M' sitting at 3a/3b sites (purple polyhedra in Figure 1c), while the divalent cations (M'') sit in 6c sites (green polyhedra). The TM-F polyhedra are connected to each other through corner sharing to form a three-dimensional open framework. There are 3 distinct sub-sites for Na occupation, namely Na1 (orange spheres in Figure 1c), Na2 (half-blue spheres), and Na3 (half-maroon spheres). There are 6 Na sites of each type in the conventional trigonal cell, with the Na2 and Na3 sites being half-occupied in the stoichiometric (i.e.,  $\text{A}_2\text{M}_2\text{F}_7$ ) weberite. All three Na sites in the trigonal structure can be occupied by Ca, and denoted as Ca1, Ca2, and Ca3 sites in the Ca-containing structures.

The Kagome-type stacking in trigonal weberite follows an 'ABC-CABC' sequence, compared to the AA sequence in orthorhombic weberite, as depicted in Figure S3a. The  $\text{A}_3\text{M}$  layer in trigonal weberite, which is constructed with four half occupied Na2 and four fully occupied Na1 sites forming an octagonal ring with a trivalent TM at the center is shown in Figure S3b. The  $\text{AM}_3$  layer consists of four divalent and two trivalent TMs forming a hexagonal ring with two half-occupied Na3 sites within the ring, as displayed in Figure S3c. For a point of comparison with the orthorhombic structure, the trigonal weberite with stoichiometric Na site occupancy (i.e., containing 2 Na per formula unit) is illustrated in Figure S4a, and the corresponding Kagome-type stacking is depicted in Figure S4b-c. The distinctions among the A-, B-, and C-type stacking layers lie in the orientation of the TMs and/or the arrangement of Na sites. For instance, Na1 sites are arranged in identical zigzag fashion along the [100], [110], and [010] directions in the  $\text{A}_3\text{M}$  layer, within the A-, B-, and C-type stacking slabs, respectively (Figure S4b). Note that the monoclinic weberite is reported to exist in two different Kagome-type stacking sequences, namely ABAB and AABBAABB with both phases crystallizing in the *C2/c* space group.<sup>73</sup> However, we do not include the monoclinic structure in our study since only the orthorhombic and trigonal weberites have demonstrated electrochemical activity in NIBs.<sup>65,67</sup>

For Ca-containing weberites, we generated the corresponding orthorhombic (O-weberite) and trigonal (T-weberite) compositions and structures (i.e.,  $\text{Ca}_x\text{M}_2\text{F}_7$ ) by substituting  $\text{Ca}^{2+}$  at the  $\text{Na}^+$  sites and utilising a redox-active 3d TM (Ti, V, Cr, Mn, Fe, Co, or Ni) at the M sites. We considered the charged and discharged weberite compositions to be  $\text{M}_2\text{F}_7$  (TM oxidation state of +3.5) and  $\text{Ca}_{1.5}\text{M}_2\text{F}_7$  (TM oxidation state of +2) to account for charge-neutrality of the overall composition given most TMs can reversibly access oxidation states between +2 and +4 during a redox reaction.<sup>48</sup> We utilised the primitive cell of O-weberite and conventional cell of T-weberite to calculate the the ground state structure at both charged and discharged compositions.

Based on calculated DFT total energies, we find the O-weberite to be energetically more favorable than the T-weberite at the charged compositions for V, Fe, and Co compounds, while the T-weberite is more favorable for charged Ti, Cr, Mn, and Ni compounds. In the case of discharged weberite compositions, we find the T-weberite structure to be energetically more favorable for all TMs considered. We have compiled the relative energies between O- and T-weberite structures at both the charged and discharged compositions in Table S2 of the SI. The occupancy of individ-

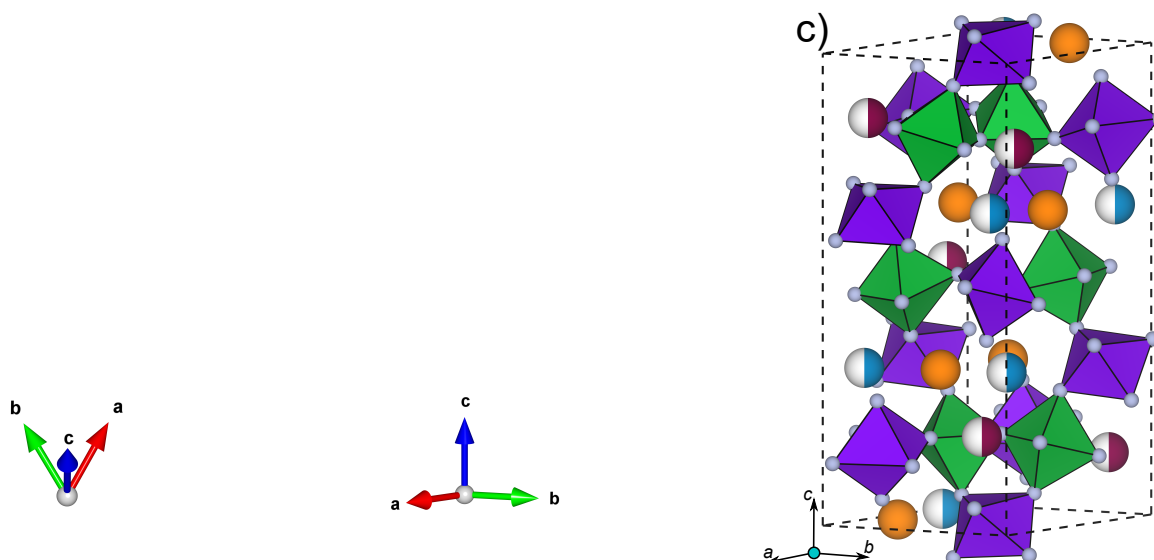


**Fig. 1** The crystal structure of the conventional cell (panel a) and primitive cell (panel b) of orthorhombic weberite, and conventional cell of trigonal weberite (panel c). Green and purple polyhedra indicate  $\text{MF}_6$  octahedral for divalent ( $\text{M}^{2+}$ ) and trivalent ( $\text{M}^{3+}$ ) transition metals, respectively, where oxygen atoms are represented by grey spheres. Orange, and light blue spheres in panel a, b, c indicate Na1 and Na2 sites (equivalent to Ca1 and Ca2 in Ca-based weberites), respectively, and maroon spheres in panel c indicate Na3 sites (equivalent to Ca3). Dashed black lines indicate the extent of the unit cell.

**Table 1** Site occupancy of the Ca1, Ca2, and Ca3 sites in the calculated T-weberite ground states.

Compositions	Ca site occupancy		
	Ca1	Ca2	Ca3
$\text{Ca}_{1.5}\text{Ti}_2\text{F}_7$	1/3	2/3	1/2
$\text{Ca}_{1.5}\text{M}_2\text{F}_7$ , M = V, Cr, Co	1/3	2/3	1/2
$\text{Ca}_{1.5}\text{M}_2\text{F}_7$ , M = Mn, Fe	2/3	1/3	1/2
$\text{Ca}_{1.5}\text{Ni}_2\text{F}_7$	1/2	1/2	1/2

ual Ca sites in the ground state weberite configurations (i.e., T-weberite for discharged compositions), as calculated by DFT, is compiled in **Table 1**, while a schematic of all ground state configurations is compiled in **Figure S5**. Interestingly, at the discharged composition, we find Ca to partially occupy all three crystallographic sites for all TMs, indicating the lack of a strong preference for a specific site. Note that although the Ca occupancies are identical for Ti and V/Cr/Co T-weberites (**Table 1**), the specific Ca-vacancy arrangements are different (**Figure S5**).

### 2.1.2 Perovskites

Similar to weberites, we consider perovskites of composition,  $\text{Ca}_x\text{MF}_3$ , obtained by inserting Ca at possible Na sites in prototypical structures. The charged and discharged compositions of Ca-containing perovskites are  $\text{MF}_3$  (TM oxidation state of +3), and  $\text{Ca}_{0.5}\text{MF}_3$  (TM oxidation state of +2), respectively, which satisfies the charge neutrality constraint. Note that Na-containing perovskite-type TM fluorides exhibit different polymorphs depending on the TM. For our investigation, we considered three different perovskite polymorphs, namely cubic ( $Pm\bar{3}m$  space group), orthorhombic ( $Pnma$ ), and triclinic ( $P\bar{1}$ ). While we used the conventional perovskite cell (containing four  $\text{Ca}_x\text{MF}_3$  formula units) for calculations involving orthorhombic and trigon-

nal polymorphs, we used a  $2 \times 2 \times 2$  supercell (with eight formula units) for the cubic polymorph. The set of perovskite structures we considered, along with the calculated ground state Ca-vacancy configurations are compiled in **Figure S6**.

For each TM, we considered the experimentally known ground state<sup>61</sup> of the corresponding Na-containing perovskite for creating the corresponding Ca-perovskite structure. For example, we used the cubic and triclinic structures for  $\text{Ca}_x\text{VF}_3$  and  $\text{Ca}_x\text{CrF}_3$ , respectively, since the ground states of the corresponding Na-containing perovskites (i.e.,  $\text{NaVF}_3$  and  $\text{NaCrF}_3$ ) are cubic<sup>74</sup> and triclinic<sup>75</sup>. Similarly, we used the orthorhombic polymorph for Mn,<sup>76</sup> Fe,<sup>77</sup> Co,<sup>78</sup> and Ni<sup>78</sup> containing perovskites. For the case of  $\text{Ca}_x\text{TiF}_3$ , we calculated the total energies of the cubic, orthorhombic, and triclinic structure with composition of  $\text{Ca}_{0.5}\text{TiF}_3$ , as the ground state of the analogous Na-containing composition is unknown. Subsequently, we found the orthorhombic structure to be energetically preferred for Ti-based perovskite (16.7 and 0.1 meV/atom lower than cubic and triclinic, respectively). For each discharged  $\text{Ca}_{0.5}\text{MF}_3$  polymorph, we constructed the corresponding charged structure by removing all  $\text{Ca}^{2+}$  from the discharged structure.

### 2.2 Thermodynamic Stabilities

**Figure 2** presents the 0 K calculated thermodynamic (in)stability, quantified using energy above or below the convex hull ( $E^{\text{Hull}}$ <sup>62</sup>), of the charged and discharged weberite (first two rows) and perovskite (last two rows) fluorides, for all TM-containing systems considered. The  $E^{\text{Hull}}$  value for each composition is indicated using a text annotation in the corresponding square of **Figure 2**, where blue (red) squares indicate stable/metastable (unstable) compositions. Note that values of  $E^{\text{Hull}} \geq 100$  meV/atom ( $E^{\text{Hull}} \leq 0$  eV/atom) are depicted by fully red (blue) squares. Given that

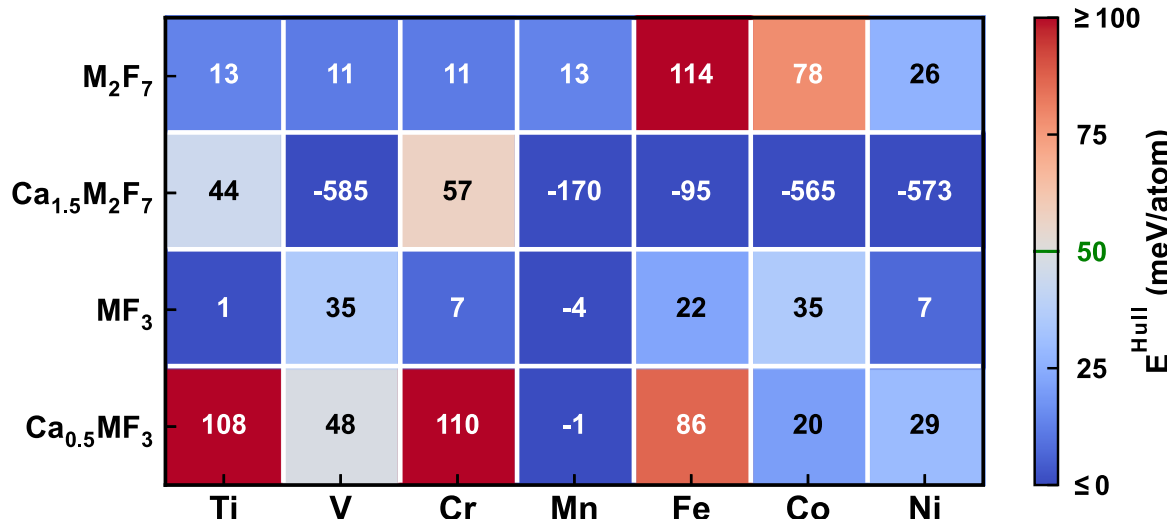


**Fig. 2** DFT-calculated energy above or below the ground-state convex hull ( $E^{Hull}$ ) for charged and discharged weberites (first two rows), and perovskites (last two rows). Each column corresponds to a specific 3d TM. Blue (red) squares indicate high degrees of stability (instability), with the specific  $E^{Hull}$  value of each composition listed as text annotation within each square. The green line on the legend bar indicates the rule-of-thumb  $E^{Hull} \sim 50$  meV/atom threshold for experimental synthesizability.

metastable compounds at 0 K can be synthesized under different experimental conditions, we have used a rule-of-thumb synthesizability threshold of  $E^{Hull} \sim 50$  meV/atom,<sup>79</sup> as indicated by the green line on the legend bar of **Figure 2**. Typically compositions with  $0 < E^{Hull} \leq 50$  meV/atom are referred to as metastable, while compositions with  $E^{Hull} > 50$  meV/atom are considered unstable. The 0 K convex hull of all ternary Ca-M-F weberites and perovskites, which comprise of possible all unary, binary, and ternary compositions that are known to exist in addition to the weberites and perovskites considered here, are compiled in **Figures S7, S8**. The compounds that are ‘adjacent’ on the convex hull for all weberites and perovskites, i.e., compounds that thermodynamically compete with stable weberites/perovskites for existence and compounds that are the decomposition products of unstable weberites/perovskites, are compiled in **Table S3**.

We observe that most of the charged compositions of weberites (first row in **Figure 2**) are metastable with  $E^{Hull}$  (in meV/atom) of 13 ( $Ti_2F_7$ ), 11 ( $V_2F_7$ ), 11 ( $Cr_2F_7$ ), 13 ( $Mn_2F_7$ ), and 26 ( $Ni_2F_7$ ), suggesting that these compounds are potentially synthesizable. In contrast, the charged Fe- and Co-weberites are unstable, exhibiting high  $E^{Hull}$  of 114 and 78 meV/atom, respectively. Note that  $Fe_2F_7$  is thermodynamically driven to decompose into the stable adjacent compounds on the Ca-Fe-F convex hull, namely  $F_2$  and  $FeF_3$  (**Table S3** and **Figure S8**). Similarly,  $Co_2F_7$  is expected to decompose into  $F_2$  and  $CoF_3$ .

Interestingly, most of the discharged weberites (second row in **Figure 2**) are stable compounds with large negative  $E^{Hull}$  (in meV/atom) of -585 ( $Ca_{1.5}V_2F_7$ ), -170 ( $Ca_{1.5}Mn_2F_7$ ), -95 ( $Ca_{1.5}Fe_2F_7$ ), -565 ( $Ca_{1.5}Co_2F_7$ ), and -573 ( $Ca_{1.5}Ni_2F_7$ ), suggesting that these compositions should be experimentally synthesizable given their large thermodynamic driving force for formation. While discharged Ti-weberite is metastable ( $E^{Hull} \sim 44$  meV/atom), the discharged Cr-weberite is marginally unstable ( $E^{Hull} \sim 57$  meV/atom, marginally higher than our syn-

thesizability threshold). Nevertheless, both  $Ca_{1.5}Ti_2F_7$  and  $Ca_{1.5}Cr_2F_7$  may be experimentally accessible. Note that we consider  $Ca_{1.5}Cr_2F_7$  to be metastable to ensure that we don’t have any false negatives, i.e., a material being erroneously not considered a possible candidate.

In the case of perovskites, most of the charged fluorides lie marginally above the convex hull and are likely synthesizable, including  $TiF_3$ ,  $VF_3$ ,  $CrF_3$ ,  $FeF_3$ ,  $CoF_3$  and  $NiF_3$ , with  $E^{Hull}$  (in meV/atom) of 1, 35, 7, 22, 35, and 7, respectively. Note that these charged perovskites are metastable with respect to their corresponding known trigonal trifluoride polymorphs (with space group of  $R\bar{3}cR$ ), as compiled in **Table S3**.<sup>80</sup> The only charged perovskite that is thermodynamically stable at 0 K is  $MnF_3$ , with  $E^{Hull}$  of -4 eV/atom. On the other hand, several discharged perovskites are unstable, with  $Ca_{0.5}TiF_3$ ,  $Ca_{0.5}CrF_3$ , and  $Ca_{0.5}FeF_3$  exhibiting large  $E^{Hull}$  values of 108, 110, and 86 meV/atom, respectively. The metastable discharged perovskites include  $Ca_{0.5}VF_3$ ,  $Ca_{0.5}CoF_3$ , and  $Ca_{0.5}NiF_3$ , with  $E^{Hull}$  of 48, 20, and 29 meV/atom, respectively. Similar to charged perovskites, the only discharged perovskite composition that is thermodynamically stable is the Mn-version, with  $E^{Hull}$  of -1 meV/atom.

Generally, it is preferable that both the charged and discharged compositions of an intercalation system are thermodynamic stable (or metastable) to prevent undesirable decomposition or conversion reactions.<sup>81</sup> Thus, we identify  $Ca_xMnF_3$  as a potential Ca-cathode, under the constraint of both charged and discharged phases being stable. Given that there are several examples of metastable cathodes that show good electrochemical performance,<sup>82–85</sup> we can use a constraint of both charged and discharged compositions being at most metastable for identification of candidates. In this context, we identify the following compositions to be candidate cathodes for CBs solely based on our 0 K stability calculations, namely,  $Ca_xTi_2F_7$ ,  $Ca_xV_2F_7$ ,  $Ca_xCr_2F_7$ ,  $Ca_xMn_2F_7$ , and  $Ca_xNi_2F_7$  within weberites

and  $\text{Ca}_x\text{VF}_3$ ,  $\text{Ca}_x\text{MnF}_3$ ,  $\text{Ca}_x\text{CoF}_3$ , and  $\text{Ca}_x\text{NiF}_3$  among perovskites. The other compounds that we predict to be stable, such as  $\text{Ca}_{1.5}\text{Fe}_2\text{F}_7$ , and  $\text{Ca}_{1.5}\text{Co}_2\text{F}_7$ , may be relevant for other non-CB applications.

### 2.3 Average Voltages and Theoretical Capacities

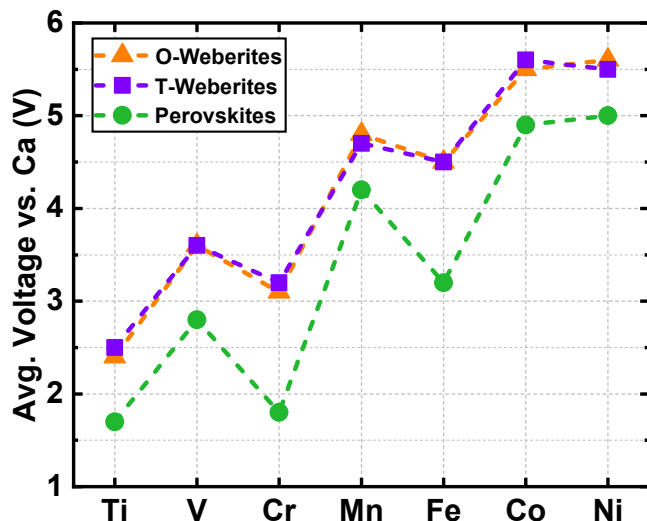


**Fig. 3** Computed average voltage as a function of transition metal, between the fully charged and discharged orthorhombic weberite (O-weberite, represented by orange triangles), trigonal weberite (T-weberite, purple squares) and perovskite (green circles) fluorides.

The electrochemical performance of a battery system is primarily quantified by its energy density, a metric determined by the voltage and capacity of electrodes utilised. Thus, we calculated the average Ca-intercalation voltage of the weberites and perovskites considered using DFT. Note that we computed the average voltage and theoretical capacity irrespective of thermodynamic (in)stabilities of all compositions to analyze the overall voltage-capacity trends. The calculated voltages (versus Ca) and gravimetric capacities are summarized in **Table 2**. The theoretical capacities are calculated with reference to the charged compositions, i.e.,  $\text{MF}_3$  for perovskites and  $\text{M}_2\text{F}_7$  for weberites. Note that the calculated capacities decrease monotonically from Ti to Ni for both fluoride frameworks, namely from 351 to 320 mAh g<sup>-1</sup> in weberites, and 255 to 231 mAh g<sup>-1</sup> in perovskites, due to the increase in atomic mass from Ti to Ni. Also, the weberites show higher theoretical capacities compared to the perovskites, due to the higher quantity of  $\text{Ca}^{2+}$  (1.5 moles in weberites versus 0.5 moles in perovskites) per formula unit that can be intercalated.

**Figure 3** displays the calculated average intercalation voltages (in Volts versus Ca metal) for all fluoride frameworks considered here. O-weberite (orange symbols), T-weberite (purple symbols) and perovskite (green symbols) represent the calculated voltages for a topotactic intercalation within the orthorhombic weberite, trigonal weberite, and perovskite polymorphs, respectively. The average voltage is calculated across the entire Ca content range, i.e.,  $\text{M}_2\text{F}_7 \leftrightarrow \text{Ca}_{1.5}\text{M}_2\text{F}_7$  for weberites and  $\text{MF}_3 \leftrightarrow \text{Ca}_{0.5}\text{MF}_3$  for perovskites. Notably, we predict the Ca intercalation voltage (in

V vs. Ca) to be within the range of 2.4 (Ti) – 5.6 (Ni) for O-weberites, 2.5 V (Ti) – 5.6 V (Co) for T-weberites, and 1.7 V (Ti) – 5.0 V (Ni) for perovskites. Clearly, the calculated voltages and trends for both O-weberite and T-weberite are similar across the 3d series, suggesting that both polymorphs may exhibit similar Ca intercalation phase behavior. Additionally, both weberites display consistently higher voltages (by at least 0.5 V) than the corresponding perovskites, which predominantly originates from the charge/discharge process accessing higher TM oxidation states in weberites (+3.5) compared to perovskites (+3).

Across the 3d series, both weberites and perovskites show similar non-monotonic trends, i.e., the voltages generally increase from Ti to Ni with local minima at Cr and Fe compositions, similar to trends observed in sulfate-NaSICONs for Ca intercalation.<sup>48</sup> In the case of T-weberites, there is a marginal dip in voltage from Co to Ni (by 0.1 V). The likely reason for the local minima in calculated voltages at Cr and Fe is the high stability of the  $\text{Cr}^{3+}$  and  $\text{Fe}^{3+}$  oxidation states, which are accessed as Ca is deintercalated. Note that  $\text{Cr}^{3+}$  and  $\text{Fe}^{3+}$  are stable due to their high-spin half-filled  $t_{2g}^3$  and half-filled d shell ( $t_{2g}^3 e_g^2$ ) electronic configurations, respectively.<sup>86,87</sup>

In addition to the topotactic voltage, we calculated the non-topotactic average voltage for select weberites that exhibit different ground state polymorphs in their charged and discharged states. For instance, the ground state of charged weberites  $\text{V}_2\text{F}_7$ ,  $\text{Fe}_2\text{F}_7$ ,  $\text{Co}_2\text{F}_7$  are orthorhombic, while the ground state of their corresponding discharged weberites ( $\text{Ca}_{1.5}\text{V}_2\text{F}_7$ ,  $\text{Ca}_{1.5}\text{Fe}_2\text{F}_7$ ,  $\text{Ca}_{1.5}\text{Co}_2\text{F}_7$ ) are the trigonal. Hence, we calculated the average voltage of V-, Fe-, and Co-based weberites between a charged orthorhombic and a discharged trigonal structure, resulting in values of 3.6, 4.5, 5.5 V vs. Ca, respectively. Importantly, the computed non-topotactic voltages are similar to the corresponding topotactic voltages (<0.1 V difference), suggesting insignificant driving force for any phase transition between the trigonal and orthorhombic structures during Ca (de)intercalation. The similarity between the non-topotactic and topotactic voltages can also be rationalised via the ‘small’ differences in the DFT-calculated total energies between the orthorhombic and trigonal structures for all TMs (see **Table S2**). Given the marginal thermodynamic driving force for a phase transition between orthorhombic and trigonal weberites during Ca (de)intercalation, we expect the topotactic pathway to be active under electrochemical conditions. Therefore, we take into account topotactic Ca (de)intercalation in the trigonal weberite for further discussions in this manuscript, given the trigonal structure is energetically preferred at the  $\text{Ca}_{1.5}\text{M}_2\text{F}_7$  composition for all TMs considered.

Given the lower voltages with Ti-based weberites and perovskites, and the Cr-perovskite ( $\leq 2.5$  V), these compositions are better suited for anode applications, while the high voltages of Co- and Ni-based fluorides ( $> 5$  V) may be beyond the stability limits of available Ca-electrolytes. Despite this concern, it may be possible to operate the Co and Ni fluorides at a reduced voltage by extracting a lower amount of Ca from the cathode, albeit reducing the energy density. For example, the calculated voltage of 4.5 V for  $\text{Fe}_2\text{F}_7 \leftrightarrow \text{Ca}_{1.5}\text{Fe}_2\text{F}_7$  decreases to 3.4 V when con-

**Table 2** The calculated average intercalation voltage (in Volts versus Ca) and the theoretical gravimetric capacity (in mAh g<sup>-1</sup>) of the weberites and perovskites considered. O-Weberites and T-weberites represent voltages calculated for topotactic intercalation within the orthorhombic and trigonal weberite polymorphs, respectively. The theoretical capacities are computed with respect to the molar mass of M<sub>2</sub>F<sub>7</sub> for weberites and MF<sub>3</sub> for perovskites (M = 3d TM).

M	Average Voltage (V)			Theoretical Capacity (mAh g <sup>-1</sup> )	
	O-Weberites	T-Weberites	Perovskites	Weberites	Perovskites
Ti	2.4	2.5	1.7	351	255
V	3.6	3.6	2.8	342	248
Cr	3.1	3.2	1.8	339	246
Mn	4.8	4.7	4.2	331	239
Fe	4.5	4.5	3.2	328	237
Co	5.5	5.6	4.9	320	231
Ni	5.6	5.5	5.0	320	231

**Table 3** Calculated Ca<sup>2+</sup> E<sub>m</sub> in perovskites considered, at charged and discharged states. Solid lines represent absence of reliable E<sub>m</sub> for MnF<sub>3</sub> and Ca<sub>0.5</sub>CoF<sub>3</sub> due to convergence difficulties.

Compounds	Migration energy (meV)	
	Charged	Discharged
Ca <sub>x</sub> VF <sub>3</sub>	2875	1832
Ca <sub>x</sub> MnF <sub>3</sub>	—	1980
Ca <sub>x</sub> CoF <sub>3</sub>	1666	—
Ca <sub>x</sub> NiF <sub>3</sub>	2445	2120

sidering Ca<sub>0.5</sub>Fe<sub>2</sub>F<sub>7</sub> ↔ Ca<sub>1.5</sub>Fe<sub>2</sub>F<sub>7</sub>, where only one mole of Ca is extracted per weberite formula unit. Thus, all weberites except Ti and all perovskites except Ti and Cr are candidate CB cathodes, based solely on our voltage calculations.

However, including both voltage and stability data reduces the set of possible candidates. For example, the low voltages of Ti- and Cr-perovskites may appear to be suitable for anode applications, but the high thermodynamic instability of the discharged Ti- and Cr-perovskites ( $E^{\text{Hull}} > 95$  meV/atom, **Figure 2**) may impede any practical deployment. Similarly, Fe-based weberites and perovskites are constrained by high instabilities of the charged and discharged compositions, respectively. In contrast, Mn-weberite, Mn-perovskite, and Ni-weberite are highly promising both due to their high voltages (>4 V) and thermodynamic (meta)stabilities. Thus, combining our voltage and stability data, we identify weberites containing Ti, V, Cr, Mn, and Ni, and perovskites containing V, Mn, Co, and Ni to be suitable for CB electrode applications. Nevertheless, the practical feasibility of any of these identified materials to function as a CB electrode depends on their corresponding bulk Ca<sup>2+</sup> diffusivities (*vide infra*).

#### 2.4 Migration Barriers

Typically, the mobility of Ca<sup>2+</sup> in solids is lower compared to monovalent active ions, such as Li<sup>+</sup>, and Na<sup>+</sup>, due to the strong electrostatic interaction of the divalent Ca<sup>2+</sup> with the neighboring anions while migrating through a host framework.<sup>20</sup> Subsequently, we computed the migration barriers (E<sub>m</sub>) of Ca<sup>2+</sup> using the nudged elastic band (NEB)<sup>88,89</sup> framework and the generalized gradient approximation (GGA)<sup>90</sup> exchange-correlation functional in the five weberite and four perovskite candidates that we had shortlisted based on our voltage and stability calculations.

Note that the diffusivity of Ca<sup>2+</sup> depends exponentially on E<sub>m</sub>, via the well-known Arrhenius relationship.<sup>91</sup>

**Figure 4** depicts the calculated E<sub>m</sub> in weberites across three different migration pathways, namely Path1 (top row), Path2 (middle row) and Path3 (bottom row) at the charged (bottom triangles) and discharged (top triangles) compositions. The individual pathways are depicted in **Figure 6**, wherein any of the three pathways can facilitate macroscopic Ca<sup>2+</sup> diffusion within the three-dimensional trigonal weberite framework. The green line on the legend bar indicates the tolerance limit of ~1000 meV for the E<sub>m</sub>, which corresponds to maintaining a reasonable electrochemical rate performance in a potential Ca-cathode.<sup>48</sup> A brown (purple) triangle in **Figure 4** represents a low (high) E<sub>m</sub> thereby indicating a facile (poor) Ca<sup>2+</sup> migration. The calculated E<sub>m</sub> in perovskites are compiled in **Table 3**. Due to convergence difficulties with our NEB calculations, we are unable to provide an accurate E<sub>m</sub> for the charged Ca<sub>x</sub>V<sub>2</sub>F<sub>7</sub> weberite along Path3 (solid black line). The minimum energy pathways for all weberite and perovskite structures are presented in **Figure S9** and **S10** of the SI, respectively.

Unsurprisingly, our calculations predict fairly high Ca<sup>2+</sup> E<sub>m</sub> for most of the weberites considered. For instance, the E<sub>m</sub> across all three paths in Ca<sub>x</sub>V<sub>2</sub>F<sub>7</sub>, at both the charged and discharged compositions are above the 1000 meV threshold, suggesting that the V-weberite is likely infeasible to be used as a CB cathode. In the case of Ti-weberite, the E<sub>m</sub> along Path1, Path2, and Path3 are within a wide range of 641 to 1929 meV. Particularly, the E<sub>m</sub> of the charged Ca<sub>x</sub>Ti<sub>2</sub>F<sub>7</sub> along Path2 (641 meV) and Path3 (880 meV), are well within the tolerance limit. However, the E<sub>m</sub> at the discharged limit are above the 1000 meV tolerance for all three paths in the discharged Ca<sub>x</sub>Ti<sub>2</sub>F<sub>7</sub> weberite, suggesting limitations with using the Ti-weberite as a CB anode. Similarly, the Ni-weberite shows reasonable E<sub>m</sub> in its charged state along Path1 (881 meV) and Path2 (1042 meV), but the E<sub>m</sub> is above the 1000 meV tolerance in the discharged state of the Ni-weberite for all pathways, making it unsuitable as a CB cathode.

In the case of Cr- and Mn-weberites, we find at least one pathway within the corresponding structures that can facilitate Ca<sup>2+</sup> diffusion. For instance, the E<sub>m</sub> in Ca<sub>x</sub>Cr<sub>2</sub>F<sub>7</sub> exceeds the 1000 meV threshold along both Path1 (842-1376 meV) and Path3 (1238-1992 meV), suggesting the unavailability of these pathways for Ca<sup>2+</sup> motion. However, the E<sub>m</sub> along Path2 is in the range of 877-1052 meV, which is only marginally above the 1000 meV tol-

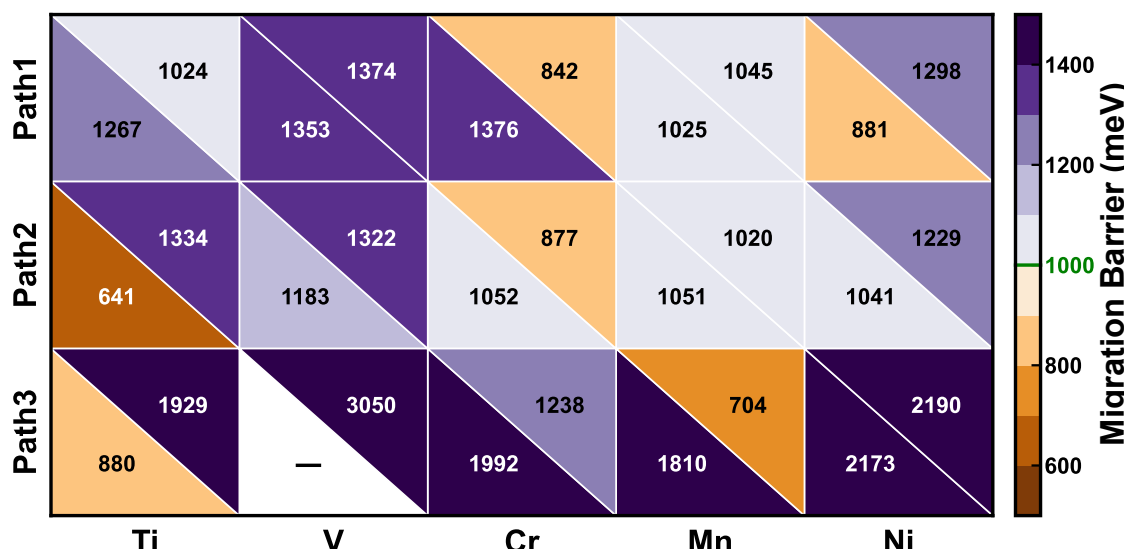


**Fig. 4** Calculated  $\text{Ca}^{2+}$   $E_m$  in the Ti-, V-, Cr-, Mn-, and Ni-weberite frameworks, indicated as text annotations. In each weberite structure, we calculated the  $E_m$  across three different migration pathways, namely Path1 (top row), Path2 (middle row), and Path3 (bottom row). Bottom and top triangles within each square indicate high (charged state) and low (discharged) Ca-vacancy concentrations. Green line on the legend bar indicates the tolerance limit on  $E_m$  ( $\sim 1000$  meV) for enabling  $\text{Ca}^{2+}$  diffusion. Due to convergence difficulties, we are unable to calculate a  $E_m$  for  $\text{V}_2\text{F}_7$  along Path3 (solid black line).

erance, suggesting that Path2 may be open for  $\text{Ca}^{2+}$  diffusion within the Cr-weberite. Considering the ground-state Ca-vacancy configuration of  $\text{Ca}_{1.5}\text{Cr}_2\text{F}_7$  trigonal weberite (Figure S5d), the fact that only Path2 remains open for  $\text{Ca}^{2+}$  diffusion possibly limits the amount of Ca that can be reversibly exchanged with the weberite structure to 0.83 moles per formula unit, corresponding to a capacity of  $\sim 164 \text{ mAhg}^{-1}$ , instead of the full 1.5 moles of Ca ( $\sim 339 \text{ mAhg}^{-1}$ ).

In the Mn-weberite, the  $E_m$  along both Path1 (1025-1045 meV) and Path2 (1020-1051 meV) are only marginally above the threshold, suggesting the feasibility of  $\text{Ca}^{2+}$  migration along both paths. However, Path3 is likely closed for  $\text{Ca}^{2+}$  motion in the Mn-weberite, since the  $E_m$  in the charged state (1810 meV) is significantly above the threshold despite the low  $E_m$  in the discharged state (704 meV). Given that two out of three pathways are active for  $\text{Ca}^{2+}$  motion in the Mn-weberite, based on the Ca-vacancy ground state configuration of  $\text{Ca}_{1.5}\text{Mn}_2\text{F}_7$  (Figure S5g), we conclude that the amount of Ca that can be reversibly exchanged is 1 mole per formula unit, corresponding to a capacity of  $\sim 212 \text{ mAhg}^{-1}$  instead of the maximum of 1.5 moles ( $\sim 331 \text{ mAhg}^{-1}$ ). Thus, we find both Cr-, and Mn-based weberites to be feasible to be used as CB cathodes, based on our combined set of thermodynamic stability, voltage, and Ca-mobility calculations.

With respect to perovskites, we find that the calculated  $E_m$  in the V-, Mn-, Co-, and Ni-based fluorides are all significantly above the 1000 meV threshold, namely 1832-2875 meV, 1980 meV, 1666 meV, and 2120-2455 meV. Therefore, despite their promising thermodynamic stability, average voltage, and theoretical capacity, we don't expect any of the perovskite fluorides to be CB cathode candidates due to their prohibitive  $\text{Ca}^{2+}$   $E_m$ . Note that we are unable to obtain reliable  $E_m$  values for charged  $\text{Ca}_x\text{MnF}_3$  and discharged  $\text{Ca}_x\text{CoF}_3$  compositions, due to convergence diffi-

culties, but we do not expect any  $E_m$  that is eventually calculated for these compositions to change our conclusions.

### 3 Discussion

In this work, we used DFT-based calculations to explore the chemical space of 3d TM-containing weberite and perovskite fluoride frameworks as potential intercalation cathodes for CBs. Specifically, we calculated the ground state Ca-vacancy configurations, 0 K thermodynamic stabilities, average intercalation voltages, theoretical capacities, and  $\text{Ca}^{2+}$   $E_m$  in several weberite and perovskite fluorides. We considered compositions of  $\text{Ca}_x\text{M}_2\text{F}_7$  for weberites (with  $0 \leq x \leq 1.5$ ), and  $\text{Ca}_x\text{MF}_3$  for perovskites (with  $0 \leq x \leq 0.5$ ), where M = Ti, V, Cr, Mn, Fe, Co, or Ni. Besides obtaining several qualitative trends in stabilities, voltages, and  $\text{Ca}^{2+}$  mobilities, we identify two weberite frameworks, namely Cr- and Mn-based compositions, to be promising Ca-cathodes.

**Figure 5** summarizes the overall performance of select weberites and fluorides considered in this work, indicated by green and blue colored symbols, respectively, by plotting their (theoretical) energy densities (in Wh/kg) versus the computed  $E_m$ . Green diamonds (blue hexagons) and green triangles (blue pentagons) indicate charged and discharged compositions, respectively, of weberites (perovskites). For comparison, we include experimental and computational data points from previous studies, as indicated by black empty circles.<sup>11,28</sup> The light blue region in **Figure 5** marks the range of tolerable migration barriers, i.e., within the  $\sim 1000$  meV threshold. We averaged the  $E_m$  of discharged and charged weberite compositions (from **Figure 4**) across all three possible pathways for plotting in **Figure 5**, except in  $\text{V}_2\text{F}_7$  where we averaged  $E_m$  over two pathways.

Importantly, the fluoride compositions identified in this work exhibit superior (theoretical) energy density compared to previ-

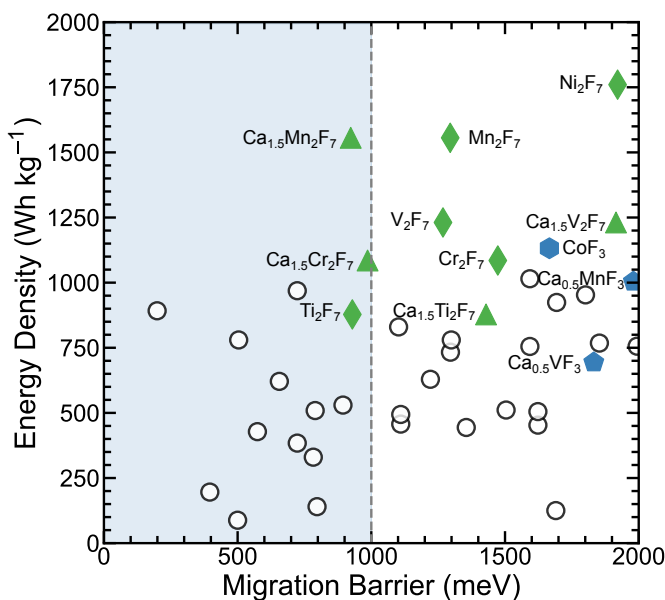


**Fig. 5** Calculated (theoretical) energy density versus migration barrier of select weberite and perovskite fluorides identified in this work. Black circles represent data from previous reports.<sup>11,28</sup>

ously reported Ca-cathodes, albeit with high  $E_m$ . Discharged Cr and Mn-based weberites fall within the range of tolerable  $E_m$ , as shown in **Figure 4**. Note that we don't consider Ti-based weberite to be a feasible candidate since the combination of charged and discharged  $E_m$  are not below the tolerance limit for any pathway within the weberite. While TMFs can exhibit promising energy densities, it is important to further mitigate the  $E_m$  exhibited by the fluorides to make them practically deployable. One strategy to reduce the  $E_m$  of TMFs, especially weberites, is to utilise multiple TMs, which can possibly introduce favorable distortions or bonding environments within the fluoride structures to reduce the Ca  $E_m$ .

Given that volume change during (de)intercalation is an important measure of cyclability of a given electrode, we computed the volume change between the fully charged and the fully discharged TMFs considered in this work, and have presented the data in **Figure S11** of SI. Except for V, we note that all TM-based weberites have lower volume change upon Ca exchange than the corresponding perovskites, further highlighting the utility of weberite frameworks. Furthermore, we computed the voltage-composition profiles for  $\text{Ca}_x\text{Cr}_2\text{F}_7$ ,  $\text{Ca}_x\text{Mn}_2\text{F}_7$ , and  $\text{Ca}_x\text{Fe}_2\text{F}_7$ , across  $x = 0, 0.5, 1$ , and  $1.5$ , and have compiled the profiles in **Figure S12**. The  $E^{\text{Hull}}$  values of the intermediate Ca-containing Cr, Mn, and Fe-weberites are included in **Table S3**.

While we employed the SCAN+U functional for average voltage and thermodynamic stability calculations, we chose GGA for  $E_m$  calculations, due to lower computational costs, better numerical convergence, and reliability in providing qualitative trends compared to SCAN.<sup>92</sup> For calculating the  $E_m$  in  $\text{Ca}_{1.5}\text{V}_2\text{F}_7$  along Path3 and  $\text{Cr}_2\text{F}_7$  along Path2, we initialized our NEB with five instead of the typical seven images since we experienced convergence difficulties with seven images. Further, in  $\text{Mn}_2\text{F}_7$  (along

Path2),  $\text{Ni}_2\text{F}_7$  (all paths),  $\text{Ca}_{0.5}\text{VF}_3$  and  $\text{MnF}_3$  we used a higher spring force constant of  $10 \text{ eV}/\text{\AA}$  between images than the usual value of  $5 \text{ eV}/\text{\AA}$  to mitigate convergence difficulties. Note that the  $E_m$  usually does not change significantly with varying the spring force constant, as demonstrated by our calculations in the discharged  $\text{Ca}_x\text{Ni}_2\text{F}_7$  system, which displays near-identical  $E_m$  of  $2190$  and  $2189$  meV (along Path3) using force constants of  $5$  and  $10 \text{ eV}/\text{\AA}$ , respectively.

Recently, Long et al., demonstrated that SCAN+U exhibits good qualitative trends in average voltages, but tends to overestimate the absolute voltage values and also the thermodynamic instabilities in Li-ion cathodes.<sup>93</sup> We expect similar overestimation of voltages and instabilities to extend to fluoride Ca-cathodes as well, which is why we used a slightly higher  $E^{\text{Hull}}$  stabilization threshold ( $\sim 50$  meV/atom) compared to previous studies ( $\sim 25$  meV/atom). Nevertheless, the majority of the fluorides considered here ( $\sim 54\%$ ) exhibit  $E^{\text{Hull}}$  lower than  $25$  meV/atom, suggesting that these fluorides should be synthesizable experimentally.

In terms of structures considered for the fluorides, we included orthorhombic and trigonal polymorphs for weberites and cubic, orthorhombic, and triclinic polymorphs for perovskites. The choice of the polymorphs for both weberites and perovskites was largely motivated by experimental and/or electrochemical observations in the Na-systems. Another constraint influencing the choice of polymorphs is the computational cost of considering different combinations of TMs and Ca-vacancy arrangements in each structure. For instance, perovskites in general can exist in tetragonal, rhombohedral, hexagonal, and monoclinic polymorphs as well,<sup>62</sup> which were not considered as possible structures here. While we hope to extend our Ca-cathode search space to other possible polymorphs in the fluoride chemical space in the future, we are optimistic that our search strategy and identification of candidates in this work are quite useful.

Although Fe-based fluoride weberite exhibits attractive electrochemical performance as a NIB cathode,<sup>67</sup> we do not find the Fe-based weberite to be a feasible candidate for CB, largely due to the instability of the charged ( $\text{Fe}_2\text{F}_7$ ) phase, which exhibits a high  $E^{\text{Hull}}$  of  $114$  meV/atom. The instability of the  $\text{Fe}_2\text{F}_7$  composition can be rationalised based on the instability of the  $4+$  oxidation state of Fe. Hence, we explored the stability of the charged Fe-weberite state with Ca already present in it such that the  $4+$  oxidation state is not accessed, i.e., a charged composition of  $\text{Ca}_{0.5}\text{Fe}_2\text{F}_7$ . Although the  $E^{\text{Hull}}$  reduces to  $71$  meV/atom with increasing Ca content in the charged state, the  $\text{Ca}_{0.5}\text{Fe}_2\text{F}_7$  phase remains above the stability threshold of  $\sim 50$  meV/atom, highlighting the instability of Fe-weberite even with introduction of significant residual Ca content in the structure.

Given the electrochemical accessibility of the charged phase,  $\text{NaFe}_2\text{F}_7$  in NIBs, and the stability of the discharged phase,  $\text{Ca}_{1.5}\text{Fe}_2\text{F}_7$ , in the Ca-Fe-F ternary space, insertion of Na within the Fe-weberite as a 'stuffing' cation may stabilize Ca-deficient compositions and enable electrochemical exchange of Ca. This is similar to the role that Na plays in the exchange of Ca in V-based NaSICON electrodes.<sup>52</sup> Also, we predict a drop in average Ca (de)intercalation voltage from  $4.5$  V in the  $\text{Fe}_2\text{F}_7$  ↔

$\text{Ca}_{1.5}\text{Fe}_2\text{F}_7$  range to 3.4 V in the  $\text{Ca}_{0.5}\text{Fe}_2\text{F}_7 \leftrightarrow \text{Ca}_{1.5}\text{Fe}_2\text{F}_7$  range, which should be in line with stability windows of existing Ca electrolytes. Thus, systems containing residual Na and/or Ca in the weberite structure may be worth exploring both computationally and experimentally.

One strategy to further explore for designing CB cathodes utilising fluoride frameworks is to explore oxyfluoride compositions, i.e., substitution of  $\text{O}^{2-}$  on F sites. Introducing a mixed anion system unlocks the potential for voltage modulation and fine-tuning other properties (such as phase behavior). Also, substituting O at F sites will likely increase the theoretical concentration of  $\text{Ca}^{2+}$  that can be accommodated in a weberite structure and potentially lower the  $E_m$  due to slightly weaker Ca-O ionic bonds than Ca-F. Another strategy is to utilise weberite structures with multiple TMs present, similar to prior studies on Na-based weberites.<sup>64,94,95</sup> For instance, Ni addition to the Cr-weberite, which is a candidate identified in this work, could enhance the voltage and mitigate  $E_m$  of  $\text{Ca}^{2+}$  since the Ni-weberite exhibits high voltage and reasonable  $E_m$  along Path1 and Path2 at the charged limit.

## 4 Conclusion

As an alternative to the state-of-the-art LIBs, Ca-based electrochemical systems are a promising pathway to develop batteries with high energy density, safety, and lower cost. However, the development of practical CBs so far has been limited by the lack of suitable cathodes. Hence, we have used DFT-based calculations to systematically explore TMFs exhibiting weberite and perovskite structures, as potential CB cathodes. Specifically, we evaluated key metrics, such as thermodynamic stabilities, average Ca-intercalation voltages, theoretical capacities, and  $\text{Ca}^{2+}$  migration barriers, across weberites of composition  $\text{Ca}_x\text{M}_2\text{F}_7$  and perovskites of composition  $\text{Ca}_x\text{MF}_3$ , where M = Ti, V, Cr, Mn, Fe, Co, or Ni. Notably, we predict a majority of the TMFs to be stable/metastable at 0 K, indicating the potential synthesizability of the TMFs considered. Our calculated average voltages exhibit higher values in weberites than perovskites, since we access higher TM oxidation states in the weberite (up to 4+) compared to perovskies (3+). Combining our stability and voltage data, we shortlisted Ti, V, Cr, Mn, and Ni weberites, and V, Mn, Co, and Ni perovskites for Ca-mobility evaluation. Subsequently, our  $E_m$  calculations indicate potential for trigonal weberites,  $\text{Ca}_x\text{Cr}_2\text{F}_7$  and  $\text{Ca}_x\text{Mn}_2\text{F}_7$ , to be candidate CB cathodes, while none of the perovskites can facilitate Ca diffusion under reasonable electrochemical conditions. We hope that our work will inspire further computational and experimental efforts into the usage of TMFs for CB cathodes, eventually resulting in the practical deployment of CBs.

## 5 Methods

### 5.1 First Principles Calculations

We used spin-polarized DFT<sup>50,51</sup> and projector augmented wave (PAW)<sup>96,97</sup> potentials, as implemented in the Vienna *ab initio* Simulation Package (VASP)<sup>98,99</sup> in all our calculations. The list of PAW potentials used in our calculations are compiled in Ta-

ble S1 of the SI. We described the valence electrons using a plane-wave basis, expanded up to a kinetic energy cutoff of 520 eV. We employed  $\Gamma$ -point-centered, Monkhorst-Pack<sup>100</sup>  $k$ -point meshes with a minimum of 48 subdivisions along each unit reciprocal lattice vector for geometry relaxations and a Gaussian smearing (of 0.05 eV) to integrate the Fermi surface. We used a Hubbard  $U$  corrected strongly constrained and appropriately normed (i.e., SCAN+ $U$ )<sup>101–105</sup> functional to describe the electronic exchange and correlation. We used  $U$  values of (in eV) 4.5 (Ti), 4.2 (V), 1.5 (Cr), 3.8 (Mn), 5.6 (Fe), and 4.0 (Co), as derived in our previous work.<sup>80</sup> We utilised total energy and force convergence criteria of  $10^{-5}$  eV and  $|0.03|$  eV/Å. For all structure relaxations, we relaxed the cell shape, volume, and ionic positions, without preserving any underlying symmetry.

### 5.2 Structure Generation

We have generated crystal structures for weberites and perovskites considered in this work by including the constraint of charge neutrality. Note that stable ionic crystals are typically charge neutral. In intercalation systems that contain 3d TMs, the oxidation state of the TM sets the limits on the content of the intercalant ion within the structure. Given that 3d TMs can reversibly change their oxidation states from +4 to +2 during (de)intercalation, the Ca content corresponding to a +4 (+2) oxidation state represents the charged (discharged) composition of the structure. For example, the highest oxidation state that a TM can acquire in a weberite is +3.5, corresponding to a composition of  $\text{Ca}_0\text{M}_2\text{F}_7$ , which in turn represents the charged state. Similarly, the lowest (+2) oxidation state that a TM can exhibit in a weberite is at a composition of  $\text{Ca}_{1.5}\text{M}_2\text{F}_7$ , which represents the discharged state. In the case of perovskites,  $\text{MF}_3$  ( $\text{M}^{3+}$ ), and  $\text{Ca}_{0.5}\text{MF}_3$  ( $\text{M}^{2+}$ ) represent the charged and discharged compositions, respectively. Thus, the maximum amount of Ca that can be exchanged per formula unit of weberite and perovskite is 1.5 and 0.5 moles, which is the value we have used in our theoretical capacity calculations of Table 2.

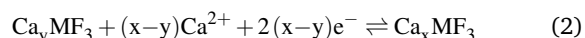
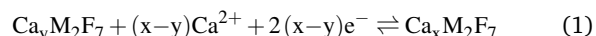
To generate structures for our DFT calculations, we obtained starting configurations from the international crystal structure database (ICSD)<sup>106</sup>. Specifically, we used the conventional cell of  $\text{Na}_2\text{Fe}_2\text{F}_7$ <sup>67</sup> as a template for trigonal weberites, while we employed the primitive cell of  $\text{Na}_2\text{NiFe}_2\text{F}_7$ <sup>107</sup> as a template for orthorhombic weberites. We substituted Fe/Ni sites in our template structures with the relevant 3d TM, while Na sites were substituted with Ca. After performing elemental substitutions, we scaled the lattice parameters of the theoretically generated structures using the "RLSVolumePredictor"<sup>108</sup> class of the pymatgen package.<sup>109</sup> Subsequently, we used the "enumlib" library<sup>110–113</sup> to generate symmetrically distinct Ca-vacancy arrangements within each structure. In total, we generated 70 trigonal- $\text{Ca}_{1.5}\text{M}_2\text{F}_7$  (10 per TM), 7 trigonal- $\text{M}_2\text{F}_7$  (one per TM), 14 orthorhombic- $\text{Ca}_{1.5}\text{M}_2\text{F}_7$  (2 per TM), and 7 orthorhombic- $\text{M}_2\text{F}_7$  (one per TM) Ca-vacancy weberite configurations.

Similar to weberites, we followed the elemental substitution, lattice parameter scaling, and Ca-vacancy ordering enumeration to generate Ca-containing fluoride perovskites. In total, we gen-

erated 35 configurations for  $\text{Ca}_{0.5}\text{MF}_3$  compositions, including 13 for Ti, 6 for V, 4 for Cr, and 3 each for Mn, Fe, Co, and Ni and 7  $\text{MF}_3$  (one per TM) configurations. Note that the discharged phase of perovskites exhibit different number of distinct Ca-vacancy configurations depending on the crystal structure. For instance, the orthorhombic  $\text{Ca}_{0.5}\text{MF}_3$  perovskite with (M = Ti, Mn, Fe, Co, or Ni) exhibits three possible Ca-vacancy configurations, while the cubic and triclinic versions exhibit six and four distinct configurations, respectively. We obtained a total of 13  $\text{Ca}_{0.5}\text{TiF}_3$  configurations since we considered all three polymorphs (i.e., cubic, orthorhombic, and triclinic) for identifying the ground state configuration of the Ti-perovskite.

### 5.3 Average Voltage Calculations

In a reversible intercalation battery, where  $\text{Ca}^{2+}$  is inserted/extracted into/from a cathode material of composition  $\text{Ca}_y\text{M}_2\text{F}_7$  (in a weberite structure) or  $\text{Ca}_y\text{MF}_3$  (in a perovskite structure), the overall redox reaction can be expressed as Eq. 1 and Eq. 2, respectively.



y and x are the concentrations of Ca in the charged and discharged weberite or perovskite fluorides, respectively. The average intercalation voltage for a given cathode material upon intercalation of (y-x) moles of Ca can be calculated using the Nernst equation (Eq. 3), as below.<sup>114</sup>

$$\langle V \rangle = -\frac{\Delta G}{2(x-y)F} \approx -\frac{E(\text{Ca}_x\text{M}_2\text{F}_7/\text{Ca}_x\text{MF}_3) - [E(\text{Ca}_y\text{M}_2\text{F}_7/\text{Ca}_y\text{MF}_3) + (x-y)\mu_{\text{Ca}}]}{2(x-y)F} \quad (3)$$

$\Delta G$  is the Gibbs energy change of the redox reaction, which is approximated as the total energy calculated using DFT ( $\Delta G \approx \Delta E$ ), ignoring the  $p - V$  and entropic contributions. F in Eq. 3 is the Faraday constant and  $\mu_{\text{Ca}}$  is the Ca chemical potential in pure Ca metal (i.e., in its ground state face-centered-cubic structure).

### 5.4 Ab initio Thermodynamics

The 0 K thermodynamic stability of the weberite and perovskite fluorides considered were evaluated with respect to the corresponding elemental, binary, and ternary compounds, as obtained from the ICSD, followed by DFT total energy calculations. For estimating stability, we exclusively considered only ordered structures that are available in the ICSD, to reduce computational complexity. In addition to the ICSD compounds, we included the theoretically obtained weberite (perovskite) compositions for estimating the stability of perovskite (weberite) compositions, since both weberites and perovskites occupy the same Ca-TM-F ternary chemical space. We used the pymatgen<sup>109</sup> package to construct

the 0 K convex hull and calculate the  $E^{\text{Hull}}$  for all Ca-TM-F ternary systems. Note that we used the SCAN functional without any  $U$  corrections for total energy calculations of all unary systems (i.e., Ca, TMs, and  $\text{F}_2$ ).

### 5.5 Migration Barrier Calculations

We used DFT-based NEB<sup>88,89</sup> to evaluate the  $\text{Ca}^{2+}$   $E_m$  in select weberite and perovskite fluorides. We used the GGA exchange-correlation functional instead of SCAN/SCAN+ $U$  to calculate  $E_m$  to minimize computational costs and mitigate convergence difficulties.<sup>92</sup> For all structures, we calculated  $E_m$  at both the charged (low Ca concentration) and the discharged (high Ca concentration) states. We considered a vacancy-mediated  $\text{Ca}^{2+}$  migration mechanism in all structures. We converged the atomic forces to  $|0.03| \text{ eV}/\text{\AA}$  within the endpoint structures of each NEB. Subsequently, we initialized the minimum energy path (MEP) of the NEB calculation by linearly interpolating the lattice vectors and atomic positions to create seven intermediate images between the endpoints, with a spring constant of  $5 \text{ eV}/\text{\AA}$  between images. For select structures, we used five intermediate images and/or a spring constant of  $10 \text{ eV}/\text{\AA}$  (see Section 3). We sampled the irreducible Brillouin zone of all endpoint and NEB calculations with  $\Gamma$ -centered Monkhorst-Pack<sup>100</sup>  $k$ -point meshes with a minimum of 32 sub-divisions across each unit reciprocal lattice vector. The NEB calculations were converged until the perpendicular component of the band force between images reduced to  $< |0.05| \text{ eV}/\text{\AA}$ .

For identifying potential Ca-cathode candidates with reasonable rate performance, we consider a fairly liberal maximum allowed  $E_m$  of  $\sim 1000 \text{ meV}$ , corresponding to a Ca (de)intercalation across cathode particles of size  $\sim 5 \text{ nm}$ , at  $333 \text{ K}$  ( $60^\circ\text{C}$ ) and C/10 rate.<sup>48</sup> Within the trigonal weberite, we identified three possible  $\text{Ca}^{2+}$  migration pathways with distinct local environments, namely Path1 (Ca1-Ca1), Path2 (Ca2-Ca1), and Path3 (Ca3-Ca1), as depicted in Figure 6. The same pathways for  $\text{Na}^+$  migration were explored by Lu et al.<sup>94</sup> in a recent study. Note that the Na arrangement along the B-type slab (within the ABCABC stacking sequence) is equivalent to the Na arrangement in the A- and C-type slabs, but along different directions. Therefore, the type of paths considered change their direction depending on the type of slab considered. For example, Path1 is along the  $a$ -axis or [100] direction in the  $\text{A}_3\text{M}$  layer of the B-type slab, which is analogous to Path1 along the [110] direction in the A-type and [010] direction in the C-type slabs.

Notably, Path1 and Path2 migration pathways lie on the  $a - b$  plane (across all A-, B-, and C-type slabs) allowing accessibility of  $\text{Ca}^{2+}$  at the Ca1 and Ca2 sites (within the  $\text{A}_3\text{M}$  layers), as shown in Figure 6a. Specifically, all the Ca1 sites can be accessed through Path 1, while the Ca at Ca2 sites can be accessed through Path2. The  $\text{Ca}^{2+}$  at Ca3 sites on the  $\text{AM}_3$  layer can migrate along Path3, if both  $E_m$  from Ca3 to Ca1 and Ca3 to Ca2 are reasonable. Note that the Ca1-Ca3-Ca2 chains along the  $c$ -axis are connected via Path3, which is independent of Path1 and Path2. In case only one  $E_m$ , i.e., Ca3-Ca1 or Ca3-Ca2, is reasonable,  $\text{Ca}^{2+}$  at Ca3 sites can migrate to available Ca1 or Ca2 sites on the  $\text{A}_3\text{M}$  layer, and subsequently use Path1 or Path2 for macroscopic diffusion.

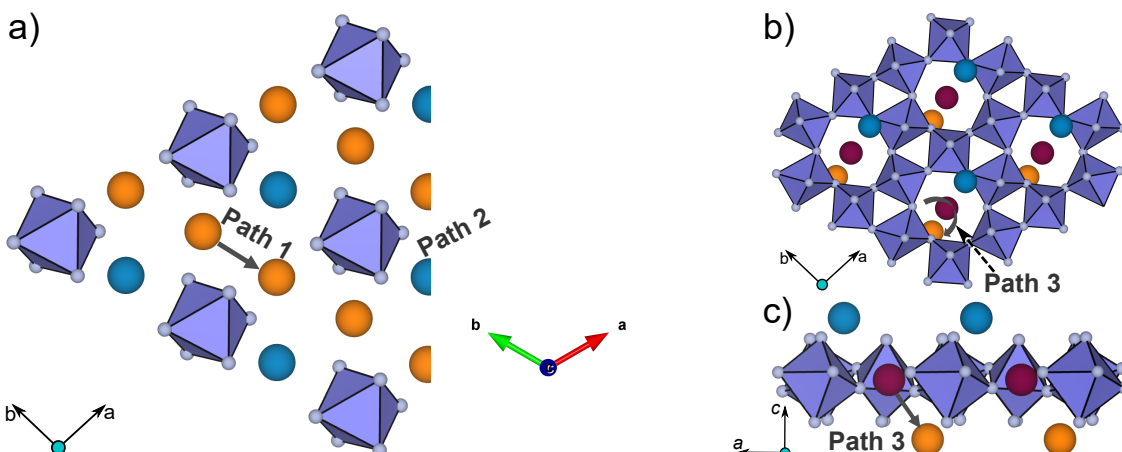


**Fig. 6**  $\text{Ca}^{2+}$  migration pathways in trigonal weberite, including Path1, Path2 (panel a), and Path3 (panels b and c). Purple polyhedra indicate  $\text{MF}_6$  octahedra and F atoms are represented by grey spheres. Orange, and light blue spheres in panel a, b, c indicate Ca1 and Ca2 sites, while maroon spheres in panel b and c indicate Ca3 sites.

However, Lu et al.<sup>94</sup> have shown that the MEP and  $E_m$  for a Na hop from Na3 to Na1 sites are similar to a Na hop from Na3 to Na2 sites. Given the similarity between the migration paths from Na3 (Ca3) to Na1 (Ca1) and Na2 (Ca2) sites, we evaluated the  $E_m$  for  $\text{Ca}^{2+}$  migration from Ca3 to Ca1 sites along Path3 (see panels b and c of **Figure 6**). Thus, depending upon the magnitude of  $E_m$ , we can conclude that either Path3 will be fully open or fully closed to Ca-diffusion.

## Author Contributions

GSG: Conceptualization, Supervision, Methodology, Writing, and Editing. DBT: Conceptualization, Data generation and curation, Visualization, Writing, and Editing.

## Conflicts of Interest

There are no conflicts to declare.

## Data Availability Statement

All the computational data presented in this work are openly available at our GitHub repository.

## Acknowledgements

G.S.G. acknowledges financial support from the Indian Institute of Science (IISc) and support from the Science and Engineering Research Board (SERB) of Government of India, under Sanction Numbers SRG/2021/000201 and IPA/2021/000007. D.B.T. acknowledges financial support from Indian Institute of Science. The authors acknowledge the computational resources provided by the Supercomputer Education and Research Centre (SERC), IISc. A portion of the calculations in this work used computational resources of the supercomputer Fugaku provided by RIKEN through the HPCI System Research Project (Project ID hp220393). We acknowledge National Supercomputing Mission (NSM) for providing computing resources of ‘PARAM Siddhi-AI’, under National PARAM Supercomputing Facility (NPSF), C-DAC, Pune, and the resources of ‘Param Utkarsh’ at CDAC Knowledge Park, Bengaluru. Both PARAM Siddhi-AI and PARAM Utkarsh are

implemented by CDAC and supported by the Ministry of Electronics and Information Technology (MeitY) and Department of Science and Technology (DST), Government of India. The authors gratefully acknowledge the computing time provided to them on the high-performance computer noctua1 and noctua2 at the NHR Center PC2. This was funded by the Federal Ministry of Education and Research and the state governments participating on the basis of the resolutions of the GWK for the national high-performance computing at universities ([www.nhr-verein.de/unsere-partner](http://www.nhr-verein.de/unsere-partner)). The computations for this research were performed using computing resources under project hpc-prf-emdf.

## References

- N. R. Van, *Nature*, 2014, **507**, 26–28.
- M. S. Whittingham, *Chemical Reviews*, 2014, **114**, 11414–11443.
- B. Nykvist and M. Nilsson, *Nature Climate Change*, 2015, **5**, 329–332.
- J.-M. Tarascon, *Nature Chemistry*, 2010, **2**, 510–510.
- D. Larcher and J.-M. Tarascon, *Nature Chemistry*, 2015, **7**, 19–29.
- Z. P. Cano, D. Banham, S. Ye, A. Hintennach, J. Lu, M. Fowler and Z. Chen, *Nature Energy*, 2018, **3**, 279–289.
- E. A. Olivetti, G. Ceder, G. G. Gaustad and X. Fu, *Joule*, 2017, **1**, 229–243.
- P. Canepa, G. Sai Gautam, D. C. Hannah, R. Malik, M. Liu, K. G. Gallagher, K. A. Persson and G. Ceder, *Chemical Reviews*, 2017, **117**, 4287–4341.
- M. R. Palacín, P. Johansson, R. Dominko, B. Dlugatch, D. Au-rbach, Z. Li, M. Fichtner, O. Lužanin, J. Bitenc, Z. Wei *et al.*, *Journal of Physics: Energy*, 2024.
- A. Ponrouch, J. Bitenc, R. Dominko, N. Lindahl, P. Johansson and M. R. Palacín, *Energy Storage Materials*, 2019, **20**, 253–262.
- M. E. Arroyo-de Dompablo, A. Ponrouch, P. Johansson and M. R. Palacín, *Chemical Reviews*, 2019, **120**, 6331–6357.

- 12 A. Ponrouch, C. Frontera, F. Bardé and M. R. Palacín, *Nature Materials*, 2016, **15**, 169–172.
- 13 R. J. Gummow, G. Vamvounis, M. B. Kannan and Y. He, *Advanced Materials*, 2018, **30**, 1801702.
- 14 H. E. Suess and H. C. Urey, *Reviews of Modern Physics*, 1956, **28**, 53.
- 15 D. Monti, A. Ponrouch, R. B. Araujo, F. Barde, P. Johansson and M. R. Palacín, *Frontiers in Chemistry*, 2019, **7**, 79.
- 16 D. Wang, X. Gao, Y. Chen, L. Jin, C. Kuss and P. G. Bruce, *Nature Materials*, 2018, **17**, 16–20.
- 17 Z. Li, O. Fuhr, M. Fichtner and Z. Zhao-Karger, *Energy & Environmental Science*, 2019, **12**, 3496–3501.
- 18 S. D. Pu, C. Gong, X. Gao, Z. Ning, S. Yang, J.-J. Marie, B. Liu, R. A. House, G. O. Hartley, J. Luo *et al.*, *ACS Energy Letters*, 2020, **5**, 2283–2290.
- 19 A. Shyamsunder, L. E. Blanc, A. Assoud and L. F. Nazar, *ACS Energy Letters*, 2019, **4**, 2271–2276.
- 20 Z. Rong, R. Malik, P. Canepa, G. Sai Gautam, M. Liu, A. Jain, K. Persson and G. Ceder, *Chemistry of Materials*, 2015, **27**, 6016–6021.
- 21 M. Smeu, M. S. Hossain, Z. Wang, V. Timoshevskii, K. H. Bevan and K. Zaghib, *Journal of Power Sources*, 2016, **306**, 431–436.
- 22 J. Wang, S. Tan, F. Xiong, R. Yu, P. Wu, L. Cui and Q. An, *Chemical communications*, 2020, **56**, 3805–3808.
- 23 G. S. Gautam, P. Canepa, R. Malik, M. Liu, K. Persson and G. Ceder, *Chemical communications*, 2015, **51**, 13619–13622.
- 24 B. Jeon, H. H. Kwak and S.-T. Hong, *Chemistry of Materials*, 2022, **34**, 1491–1498.
- 25 X. Zhang, X. Xu, B. Song, M. Duan, J. Meng, X. Wang, Z. Xiao, L. Xu and L. Mai, *Small*, 2022, **18**, 2107174.
- 26 S. J. Richard Prabakar, A. B. Ikhe, W.-B. Park, D. Ahn, K.-S. Sohn and M. Pyo, *Advanced Functional Materials*, 2023, **33**, 2301399.
- 27 X. Xu, M. Duan, Y. Yue, Q. Li, X. Zhang, L. Wu, P. Wu, B. Song and L. Mai, *ACS Energy Letters*, 2019, **4**, 1328–1335.
- 28 W. Lu, J. Wang, G. Sai Gautam and P. Canepa, *Chemistry of Materials*, 2021, **33**, 5809–5821.
- 29 A. P. Black, C. Frontera, A. Torres, M. Recio-Poo, P. Rozier, J. D. Forero-Saboya, F. Fauth, E. Urones-Garrote, M. E. Arroyo-de Dompablo and M. R. Palacín, *Energy Storage Materials*, 2022, **47**, 354–364.
- 30 P. A. Chando, S. Chen, J. M. Shellhamer, E. Wall, X. Wang, R. Schuarca, M. Smeu and I. D. Hosein, *Chemistry of Materials*, 2023, **35**, 8371–8381.
- 31 M. Cabello, F. Nacimiento, R. Alcántara, P. Lavela, C. Pérez Vicente and J. L. Tirado, *Chemistry of Materials*, 2018, **30**, 5853–5861.
- 32 T. Tojo, H. Tawa, N. Oshida, R. Inada and Y. Sakurai, *Journal of Electroanalytical Chemistry*, 2018, **825**, 51–56.
- 33 M. S. Chae, H. H. Kwak and S.-T. Hong, *ACS Applied Energy Materials*, 2020, **3**, 5107–5112.
- 34 T. N. Vo, H. Kim, J. Hur, W. Choi and I. T. Kim, *Journal of materials chemistry A*, 2018, **6**, 22645–22654.
- 35 M. Cabello, F. Nacimiento, J. R. González, G. Ortiz, R. Alcántara, P. Lavela, C. Pérez-Vicente and J. L. Tirado, *Electrochemistry Communications*, 2016, **67**, 59–64.
- 36 H. Park, C. J. Bartel, G. Ceder and P. Zapol, *Advanced Energy Materials*, 2021, **11**, 2101698.
- 37 A. L. Lipson, S. Kim, B. Pan, C. Liao, T. T. Fister and B. J. Ingram, *Journal of Power Sources*, 2017, **369**, 133–137.
- 38 D. S. Tchitchevova, A. Ponrouch, R. Verrelli, T. Broux, C. Frontera, A. Sorrentino, F. Bardé, N. Biskup, M. E. Arroyo-de Dompablo and M. R. Palacín, *Chemistry of Materials*, 2018, **30**, 847–856.
- 39 J. Wang, J. Wang, Y. Jiang, F. Xiong, S. Tan, F. Qiao, J. Chen, Q. An and L. Mai, *Advanced Functional Materials*, 2022, **32**, 2113030.
- 40 N. Kuperman, P. Padigi, G. Goncher, D. Evans, J. Thiebes and R. Solanki, *Journal of Power Sources*, 2017, **342**, 414–418.
- 41 T. Shiga, H. Kondo, Y. Kato and M. Inoue, *The Journal of Physical Chemistry C*, 2015, **119**, 27946–27953.
- 42 P. Padigi, G. Goncher, D. Evans and R. Solanki, *Journal of Power Sources*, 2015, **273**, 460–464.
- 43 T. Tojo, Y. Sugiura, R. Inada and Y. Sakurai, *Electrochimica Acta*, 2016, **207**, 22–27.
- 44 A. L. Lipson, B. Pan, S. H. Lapidus, C. Liao, J. T. Vaughney and B. J. Ingram, *Chemistry of Materials*, 2015, **27**, 8442–8447.
- 45 S. Kim, L. Yin, M. H. Lee, P. Parajuli, L. Blanc, T. T. Fister, H. Park, B. J. Kwon, B. J. Ingram, P. Zapol, R. F. Klie, K. Kang, L. F. Nazar, S. H. Lapidus and J. T. Vaughney, *ACS Energy Letters*, 2020, **5**, 3203–3211.
- 46 B. Jeon, J. W. Heo, J. Hyoung, H. H. Kwak, D. M. Lee and S.-T. Hong, *Chemistry of Materials*, 2020, **32**, 8772–8780.
- 47 Z.-L. Xu, J. Park, J. Wang, H. Moon, G. Yoon, J. Lim, Y.-J. Ko, S.-P. Cho, S.-Y. Lee and K. Kang, *Nature communications*, 2021, **12**, 3369.
- 48 D. B. Tekliye, A. Kumar, X. Weihang, T. D. Mercy, P. Canepa and G. Sai Gautam, *Chemistry of Materials*, 2022, **34**, 10133–10143.
- 49 G. Sai Gautam, P. Canepa, W. D. Richards, R. Malik and G. Ceder, *Nano Letters*, 2016, **16**, 2426–2431.
- 50 P. Hohenberg and W. Kohn, *Physical review*, 1964, **136**, B864.
- 51 W. Kohn and L. J. Sham, *Physical review*, 1965, **140**, A1133.
- 52 L. E. Blanc, Y. Choi, A. Shyamsunder, B. Key, S. H. Lapidus, C. Li, L. Yin, X. Li, B. Gwalani, Y. Xiao, C. J. Bartel, G. Ceder and L. F. Nazar, *Chemistry of Materials*, 2023, **35**, 468–481.
- 53 R. Bralsford, P. Harris and W. C. Price, *Proceedings of the Royal Society of London. Series A. Mathematical and Physical Sciences*, 1960, **258**, 459–469.
- 54 A. Padhi, V. Manivannan and J. Goodenough, *Journal of the Electrochemical Society*, 1998, **145**, 1518.
- 55 X. Hua, A. S. Eggeman, E. Castillo-Martínez, R. Robert, H. S. Geddes, Z. Lu, C. J. Pickard, W. Meng, K. M. Wiaderek, N. Pereira *et al.*, *Nature materials*, 2021, **20**, 841–850.
- 56 X. Fan, E. Hu, X. Ji, Y. Zhu, F. Han, S. Hwang, J. Liu, S. Bak,

- Z. Ma, T. Gao *et al.*, *Nature communications*, 2018, **9**, 2324.
- 57 B. Ouyang, N. Artrith, Z. Lun, Z. Jadidi, D. A. Kitchaev, H. Ji, A. Urban and G. Ceder, *Advanced Energy Materials*, 2020, **10**, 1903240.
- 58 R. Clément, Z. Lun and G. Ceder, *Energy & Environmental Science*, 2020, **13**, 345–373.
- 59 I. D. Gocheva, M. Nishijima, T. Doi, S. Okada, J.-i. Yamaki and T. Nishida, *Journal of Power Sources*, 2009, **187**, 247–252.
- 60 A. Kitajou, Y. Ishado, T. Yamashita, H. Momida, T. Oguchi and S. Okada, *Electrochimica Acta*, 2017, **245**, 424–429.
- 61 N. Dimov, A. Nishimura, K. Chihara, A. Kitajou, I. D. Gocheva and S. Okada, *Electrochimica Acta*, 2013, **110**, 214–220.
- 62 G. Sai Gautam, E. B. Stechel and E. A. Carter, *Chemistry of Materials*, 2020, **32**, 9964–9982.
- 63 R. B. Wexler, G. S. Gautam, R. T. Bell, S. Shulda, N. A. Strange, J. A. Trindell, J. D. Sugar, E. Nygren, S. Sainio, A. H. McDaniel *et al.*, *Energy & Environmental Science*, 2023, **16**, 2550–2560.
- 64 H. Euchner, O. Clemens and M. A. Reddy, *npj Computational Materials*, 2019, **5**, 31.
- 65 U. K. Dey, N. Barman, S. Ghosh, S. Sarkar, S. C. Peter and P. Senguttuvan, *Chemistry of Materials*, 2019, **31**, 295–299.
- 66 A. Ghosh, D. B. Tekliye, E. E. Foley, V. R. Reddy, R. J. Clémenta, G. Sai Gautam and P. Senguttuvan, *Under review*, 2024.
- 67 H. Park, Y. Lee, M.-k. Cho, J. Kang, W. Ko, Y. H. Jung, T.-Y. Jeon, J. Hong, H. Kim, S.-T. Myung *et al.*, *Energy & Environmental Science*, 2021, **14**, 1469–1479.
- 68 R. T. Shannon and C. T. Prewitt, *Acta Crystallographica Section B: Structural Crystallography and Crystal Chemistry*, 1969, **25**, 925–946.
- 69 R. D. Shannon, *Acta crystallographica section A: crystal physics, diffraction, theoretical and general crystallography*, 1976, **32**, 751–767.
- 70 O. Knop, T. S. Cameron and K. Jochem, *Journal of Solid State Chemistry*, 1982, **43**, 213–221.
- 71 L. Cai and J. C. Nino, *Acta Crystallographica Section B: Structural Science*, 2009, **65**, 269–290.
- 72 O. Yakubovich, V. Urusov, W. Massa, G. Frenzen and D. Babbel, *Zeitschrift für anorganische und allgemeine Chemie*, 1993, **619**, 1909–1919.
- 73 I. Grey, W. Mumme, T. Ness, R. S. Roth and K. Smith, *Journal of Solid State Chemistry*, 2003, **174**, 285–295.
- 74 M. Shafer, *Materials Research Bulletin*, 1969, **4**, 905–912.
- 75 F. L. Bernal, J. Sottmann, D. S. Wragg, H. Fjellvåg, Ø. S. Fjellvåg, C. Drathen, W. A. Ślawiński and O. M. Løvvik, *Physical Review Materials*, 2020, **4**, 054412.
- 76 A. Ratuszna, K. Majewska and T. Lis, *Acta Crystallographica Section C: Crystal Structure Communications*, 1989, **45**, 548–551.
- 77 G. Benner and R. Hoppe, *Journal of fluorine chemistry*, 1990, **46**, 283–295.
- 78 H. Yusa, Y. Shirako, M. Akaogi, H. Kojitani, N. Hirao, Y. Ohishi and T. Kikegawa, *Inorganic Chemistry*, 2012, **51**, 6559–6566.
- 79 W. Sun, S. T. Dacek, S. P. Ong, G. Hautier, A. Jain, W. D. Richards, A. C. Gamst, K. A. Persson and G. Ceder, *Science advances*, 2016, **2**, e1600225.
- 80 D. B. Tekliye and G. S. Gautam, *arXiv preprint arXiv:2401.10832*, 2024.
- 81 D. C. Hannah, G. Sai Gautam, P. Canepa and G. Ceder, *Advanced Energy Materials*, 2018, **8**, 1800379.
- 82 G. Sai Gautam, P. Canepa, A. Abdellahi, A. Urban, R. Malik and G. Ceder, *Chemistry of Materials*, 2015, **27**, 3733–3742.
- 83 G. Amatucci, J. Tarascon and L. Klein, *Journal of The Electrochemical Society*, 1996, **143**, 1114.
- 84 D. Aurbach, Z. Lu, A. Schechter, Y. Gofer, H. Gizbar, R. Turge man, Y. Cohen, M. Moshkovich and E. Levi, *Nature*, 2000, **407**, 724–727.
- 85 R. Malik, A. Abdellahi and G. Ceder, *Journal of the electrochemical society*, 2013, **160**, A3179.
- 86 R. Vargas and M. Galván, *The Journal of Physical Chemistry*, 1996, **100**, 14651–14654.
- 87 S. I. Shupack, *Environmental Health Perspectives*, 1991, **92**, 7–11.
- 88 G. Henkelman and H. Jónsson, *The Journal of chemical physics*, 2000, **113**, 9978–9985.
- 89 D. Sheppard, R. Terrell and G. Henkelman, *The Journal of chemical physics*, 2008, **128**.
- 90 J. P. Perdew, K. Burke and M. Ernzerhof, *Physical review letters*, 1996, **77**, 3865.
- 91 Y. Gao, T. P. Mishra, S.-H. Bo, G. Sai Gautam and P. Canepa, *Annual Review of Materials Research*, 2022, **52**, 129–158.
- 92 R. Devi, B. Singh, P. Canepa and G. Sai Gautam, *npj Computational Materials*, 2022, **8**, 160.
- 93 O. Y. Long, G. S. Gautam and E. A. Carter, *Physical Chemistry Chemical Physics*, 2021, **23**, 24726–24737.
- 94 T. Lu, S. Meng and M. Liu, *arXiv preprint arXiv:2310.04222*, 2023.
- 95 J. Liao, J. Han, J. Xu, Y. Du, Y. Sun, L. Duan and X. Zhou, *Chemical Communications*, 2021, **57**, 11497–11500.
- 96 G. Kresse and D. Joubert, *Physical Review B*, 1999, **59**, 1758.
- 97 P. E. Blöchl, O. Jepsen and O. K. Andersen, *Physical Review B*, 1994, **49**, 16223.
- 98 G. Kresse and J. Hafner, *Physical review B*, 1993, **47**, 558.
- 99 G. Kresse and J. Furthmüller, *Physical Review B*, 1996, **54**, 11169.
- 100 H. J. Monkhorst and J. D. Pack, *Physical Review B*, 1976, **13**, 5188.
- 101 J. Sun, A. Ruzsinszky and J. P. Perdew, *Physical Review Letters*, 2015, **115**, 036402.
- 102 S. L. Dudarev, G. A. Botton, S. Y. Savrasov, C. Humphreys and A. P. Sutton, *Physical Review B*, 1998, **57**, 1505.
- 103 V. I. Anisimov, J. Zaanen and O. K. Andersen, *Physical Review B*, 1991, **44**, 943.
- 104 G. S. Gautam and E. A. Carter, *Physical Review Materials*, 2018, **2**, 095401.

- 105 O. Y. Long, G. S. Gautam and E. A. Carter, *Physical Review Materials*, 2020, **4**, 045401.
- 106 M. Hellenbrandt, *Crystallography Reviews*, 2004, **10**, 17–22.
- 107 Y. Laligant, Y. Calage, G. Heger, J. Pannetier and G. Ferey, *Journal of Solid State Chemistry*, 1989, **78**, 66–77.
- 108 I.-H. Chu, S. Roychowdhury, D. Han, A. Jain and S. P. Ong, *Computational Materials Science*, 2018, **146**, 184–192.
- 109 S. P. Ong, W. D. Richards, A. Jain, G. Hautier, M. Kocher, S. Cholia, D. Gunter, V. L. Chevrier, K. A. Persson and G. Ceder, *Computational Materials Science*, 2013, **68**, 314–319.
- 110 G. L. Hart and R. W. Forcade, *Physical Review B*, 2008, **77**, 224115.
- 111 G. L. Hart and R. W. Forcade, *Physical Review B*, 2009, **80**, 014120.
- 112 G. L. Hart, L. J. Nelson and R. W. Forcade, *Computational Materials Science*, 2012, **59**, 101–107.
- 113 W. S. Morgan, G. L. Hart and R. W. Forcade, *Computational Materials Science*, 2017, **136**, 144–149.
- 114 F. Zhou, M. Cococcioni, C. A. Marianetti, D. Morgan and G. Ceder, *Physical Review B*, 2004, **70**, 235121.

Data Availability Statement for “Fluoride Frameworks as Potential Calcium Battery Cathodes” (TA-ART-04-2024- 002426)

View Article Online  
DOI: 10.1039/DTA02426E

All the computational data presented in this work are openly available at our [GitHub](#) repository.